aerospace

MDPI

Article

Dynamics Modeling and Nonlinear Optimal Control of an Underactuated Dual-Unmanned Aerial Helicopters Slung Load System

Yanhua Han [1,*], Ruofan Li [1] and Yong Zhang [2]

[1] College of Astronautics, Nanjing University of Aeronautics and Astronautics, Nanjing 211106, China; liruofan1@nuaa.edu.cn
[2] Unmanned Aerial Vehicles Research Institute, Nanjing University of Aeronautics and Astronautics, Nanjing 210016, China; yongzhang@nuaa.edu.cn
* Correspondence: hanyanhua@nuaa.edu.cn

Abstract

This paper focuses on the dynamics modeling and control methods for an underactuated Dual-Unmanned Aerial Helicopter Slung Load System (DUH-SLS), which consists of two Unmanned Aerial Helicopters (UAHs) connected to the suspended load via two sling cables. The DUH-SLS is a multi-body coupled system with internal ideal constraint forces and has seven motion degrees of freedom (DOFs) in the longitudinal plane. In this paper, a set of independent and complete generalized coordinates is selected to describe the system's motion. The dynamics model of DUH-SLS is established using Lagrange analytical mechanics. This approach, which avoids system internal forces, greatly improves modeling efficiency. Finally, the correctness of this dynamics model is validated using a virtual prototype of the DUH-SLS developed in the multi-body dynamics simulation software ADAMS. The DUH-SLS is a complex nonlinear controlled object, and the iterative Linear Quadratic Regulator (iLQR) method is introduced to design an integrated optimal controller to achieve trajectory tracking and swing suppression for the DUH-SLS. This method transforms the quadratic optimal control problem of nonlinear systems into a series of linear quadratic optimal control (LQR) problems through iterative optimization in function space, thus obtaining an optimal solution. The iLQR optimal controller requires offline iterative computation, but the optimal control obtained has a state feedback closed-loop form, which ensures robustness during online control. Numerical simulation results demonstrate that the proposed iLQR optimal controller exhibits excellent control performance in complex multi-task scenarios. Particularly in trajectory tracking tasks, the maximum average position tracking error of the iLQR controller is only 0.14 m, compared to 3.57 m and 3.11 m for the LQR and LMC (Lyapunov Method Controller) controllers, respectively. Furthermore, the controller demonstrates strong robustness against internal parameter perturbations and external complex wind disturbances, fully validating the effectiveness and superiority of the proposed approach.

Keywords: Unmanned Aerial Helicopter; helicopter slung load system; multi-body coupled dynamics; iLQR method; nonlinear optimal control

Check for updates

Received: 9 February 2026
Revised: 20 March 2026
Accepted: 31 March 2026
Published: 1 April 2026

Copyright: © 2026 by the authors. Licensee MDPI, Basel, Switzerland. This article is an open access article distributed under the terms and conditions of the Creative Commons Attribution (CC BY) license.

1. Introduction

Helicopter slung load transportation began as early as the 1950s, with emergency rescue and forest firefighting being among the main civilian applications of helicopter

slung load systems (HSLSs) [1,2]. However, when helicopters perform slung load missions, the oscillation of the airframe can cause a coupled swing between the helicopter and the suspended load [3], which severely affects the stability and safety of the HSLS. Many researchers have proposed various swing suppression algorithms to address this issue [4,5]. In recent years, with the rapid advancement of unmanned aerial vehicle technology, cooperative multi-UAV slung load transportation has become increasingly vital in both civilian and military applications, including heavy cargo delivery, disaster relief, and aerial supply missions [6]. Compared with a single UAH, the use of multiple UAHs in cooperative slung load transportation offers significant advantages, including greatly improved load capacity, maneuverability, and fault tolerance. The quantity of UAHs can also be flexibly adjusted according to the requirements of the task load, enabling efficient allocation of resources and economic benefits [7,8]. However, as the scale of the model and the dimensionality of variables increase, the complexity and difficulty of dynamics modeling and controller design for slung load systems involving multiple UAHs increase significantly. Therefore, this paper concentrates on the dynamics modeling and control methods for the Dual-Unmanned Aerial Helicopter Slung Load System (DUH-SLS), aiming to offer theoretical support and technical guidance for cooperative slung load transportation using multiple UAHs. At present, research on DUH-SLS mainly focuses on topics such as dynamics modeling, trajectory tracking, trajectory planning, and swing suppression [9,10].

There have been many studies on the dynamics modeling of HSLS at present. Refs. [11,12] established a general dynamics model for HSLS based on D'Alembert's principle and the principle of virtual work, covering various slung load configurations such as single-helicopter single-point slung load, multi-point slung load, and dual-helicopter slung load. This research selected generalized coordinates and systematically derived the dynamics equations for HSLS, providing an important reference for modeling complex slung load systems and conducting preliminary studies on DUH-SLS's dynamics. The dynamics models of multi-UAH slung load systems established in Refs. [7,13] treated the suspended load as an external disturbance, without fully considering the dynamics coupling between the suspended load and the UAH, nor incorporating the dynamic characteristics of the suspended load itself. Therefore, these models have some limitations and cannot fully reflect the dynamic characteristics of the system. In Ref. [14], the suspended load is simplified as a point mass model in the dynamics modeling of the multi-UAH slung load system. However, in practice, multi-UAH slung load systems often transport large-volume and heavy-mass cargoes, and the point mass model cannot describe the attitude characteristics of the suspended load. Ref. [15] coupled the motion of the helicopter and the suspended load by modeling the dynamics of elastic suspension cables, thereby establishing a dynamic model for the multi-UAH system. This approach took into account a wide range of factors and offered a certain degree of generality. However, the effectiveness of this modeling method was compromised when the internal forces within the multi-helicopter slung load system could not be measured. Refs. [16,17] treated UAHs as point masses and did not consider the coupling effect of the suspended load on the UAH's attitude. They established dynamics models for multi-UAH slung load systems under different slung configurations based on Lagrange analytical mechanics. In summary, there are mainly three modeling methods for multi-UAH slung load systems: the Udwadia–Kalaba equation [18], the Newton–Euler method, and the Lagrange analytical mechanics method. As the quantity of UAHs in the system increases and the constraints between UAHs become more complex, the derivation and solution process of the dynamics equations based on the Udwadia–Kalaba method becomes cumbersome. Similarly, although the Newton–Euler method can clearly describe the internal interaction forces of the system, it is computationally complex, and the derivation process is tedious. In contrast, by conducting energy analysis, Lagrange analytical

mechanics simplifies modeling, does not require consideration of ideal constraint forces within the system, and is more suitable for dynamics modeling of multi-body systems.

In practical applications, multi-UAH cooperative slung load systems often encounter issues such as suspended load swing and multi-UAH cooperative flight, which directly impact the stability, safety, and efficiency of mission execution. Therefore, it is necessary to study swing suppression and trajectory tracking control methods for DUH-SLS to ensure stability and safety in complex task scenarios. Refs. [18,19] designed nonlinear swing suppression controllers for DUH-SLS based on the Lyapunov stability principle. Simulation results showed that this method could effectively suppress the swinging of the suspended load. Ref. [17] proposed a nonlinear robust control strategy combining the integral of the sign of the error (RISE) and geometric control for multi-UAH slung load systems. This approach aims to compensate for unknown external disturbances and achieve precise control of the load's position. Simulation results showed that this strategy can achieve accurate trajectory tracking. Ref. [20] designed a distributed control scheme that ensures UAHs in the desired flying formation while effectively suppressing load swinging. Ref. [21] designed a trajectory planning scheme based on a value-function approximation algorithm, which generated the desired trajectory and passed it to the quadrotor UAV controller to achieve trajectory tracking. Simulation results showed that the trained parameters could effectively approximate the value function, and the suspended load could be stably transported from the starting position to the target position, solving the trajectory planning problem for three-UAV cooperative slung load transportation. Ref. [22] fully considered the dynamic characteristics and tension constraints of the suspended load. They used a tension distribution algorithm to generate and optimize the flight trajectory for multi-UAH systems. Recent studies have further explored more complex cooperative scenarios and control methodologies. Ref. [23] proposed an event-triggered formation optimization approach for multi-quadrotor cooperative slung load systems, dynamically adjusting formation to reduce power consumption during load transportation. Ref. [24] developed a barrier Lyapunov function-based nonlinear cooperative controller for dual-quadrotor slung load systems, constraining the relative distance between two helicopters to mitigate collision risks. Ref. [25] presented a tube-based robust model predictive controller for disturbed quadrotor slung load systems, simultaneously controlling UAV position and load swing angles while avoiding both dynamic and static obstacles. Ref. [26] extended the investigation to experimental validation, proposing a trajectory-based whole-body motion planning framework that enables agile and high-speed maneuvers for multi-UAV cooperative slung load systems, achieving accelerations eight times higher than state-of-the-art methods. Despite these contributions, previous studies have largely focused on individual control objectives in multi-UAH slung load systems, such as swing suppression, trajectory planning, or formation maintenance, without fully addressing the integrated challenge of simultaneously achieving high-precision trajectory tracking and effective load swing suppression under complex mission scenarios. How to ensure accurate tracking of complex trajectories while effectively mitigating load swing in multi-UAV cooperative slung load systems remains a compelling research problem. This paper addresses this issue by investigating a dual-UAH cooperative slung load control strategy under an underactuated configuration. The proposed approach enables simultaneous position tracking and swing suppression, demonstrating satisfactory control performance even in complex trajectory tracking tasks.

Ref. [27] first proposed the iterative Linear Quadratic Regulator (iLQR) algorithm to solve the optimal control problem for nonlinear controlled objects. It is well recognized that solving the optimal control problem for nonlinear systems is highly challenging, regardless of whether direct or indirect methods are employed. Indirect approaches typically

transform the problem into a two-point boundary value problem for nonlinear differential equations, which lack analytical solutions and are difficult to solve numerically. Even when a numerical solution is attainable, the resulting optimal control is open-loop and thus lacks robustness for real-time applications. The iLQR algorithm provides an effective alternative for nonlinear systems optimal control problems with quadratic performance indices (NLQR) [27–30]. The principle of the iLQR method is as follows: the state equation of the controlled system is linearized by small perturbations along the state and control trajectories, resulting in an approximate linear nonhomogeneous system. Combined with the quadratic performance index, this forms an LQR problem. Due to LQR problems being relatively straightforward to solve, the optimal control and corresponding state trajectories can be readily obtained. The original nonlinear system is then linearized along these trajectories, yielding a new LQR problem. This new LQR problem is subsequently solved to update the control and state trajectories again. This iterative process is repeated until the convergence criterion is satisfied, at which point the control function obtained in the final iteration is the optimal solution to the NLQR problem. Moreover, this optimal control is inherently in closed-loop form, ensuring robustness during online control. Theoretically, Ref. [31] provided rigorous convergence guarantees for iLQR, establishing both global convergence to stationary points and local linear convergence rates, which further justifies its applicability to nonlinear control problems. The iLQR framework has been further advanced in recent studies. Ref. [32] developed an iLQR-based model predictive control approach for tilt-propulsion UAVs, demonstrating superior performance over conventional methods. Ref. [33] extended iLQR to hybrid systems through a hybrid iLQR MPC framework for legged robots, validating its applicability to complex dynamical systems with contact events. Building upon these developments, this paper applies the iLQR algorithm to the dual-helicopter slung load system—a complex nonlinear dynamical system—to achieve simultaneous trajectory tracking and swing suppression.

The main contributions of this paper are summarized as follows: First, a set of independent and complete generalized coordinates for the DUH-SLS is skillfully selected, and a seven-degree-of-freedom dynamics model is established based on Lagrange analytical mechanics. By avoiding the computation of ideal internal constraint forces, this approach significantly enhances the modeling efficiency of multi-body coupled systems, and the correctness of the theoretical modeling is verified through comparative studies with the ADAMS virtual prototype, laying a solid foundation for subsequent controller design. Second, to achieve simultaneous trajectory tracking and swing suppression, the iLQR method is introduced to design an integrated optimal controller for the DUH-SLS. To fully exploit the advantages of iLQR, we design an initialization strategy based on LQR simulation results, enabling the iterative process to converge within only 1–2 iterations, thus achieving a balance between optimality and real-time feasibility. Furthermore, to comprehensively validate the proposed method, a virtual prototype of the DUH-SLS is constructed in ADAMS to verify the correctness of the dynamics model, and extensive comparisons with traditional LQR (Linear Quadratic Regulator) and LMC (Lyapunov Method Controller) controllers are conducted under various complex working conditions. Simulation results demonstrate that the designed iLQR controller exhibits superior performance in terms of tracking accuracy, swing suppression, and robustness.

To facilitate reading and comprehension, the key abbreviations used throughout this paper are summarized in Table 1. The abbreviated forms will be used directly in the following sections.

Table 1. Abbreviation table of proper nouns.

Abbreviation	Full Name
DUH-SLS	Dual-Unmanned Aerial Helicopter Slung Load System
UAH	Unmanned Aerial Helicopter
DOF	Degree of Freedom
iLQR	iterative Linear Quadratic Regulator
LQR	Linear Quadratic Regulator
LMC	Lyapunov Method Controller
ADAMS	Automatic Dynamic Analysis of Mechanical Systems

2. Dynamics Modeling of DUH-SLS

The DUH-SLS studied in this paper consists of UAH1 and UAH2, which are respectively connected to the suspended load via sling cables. In many engineering application scenarios, the motion of the DUH-SLS in the longitudinal plane is predominant. Therefore, this paper focuses only on the motion and control issues of the DUH-SLS in the longitudinal plane. The following assumptions are made before dynamics modeling.

(1) The DUH-SLS adopts a tandem slung load arrangement [8], and the fuselage structures of UAH1 and UAH2 are identical.

(2) The suspended load is a rod-shaped load [16], considering its centroid translational motion and attitude pitch motion;

(3) Both sling cables remain taut at all times, which are regarded as the lightweight cables with negligible elasticity;

(4) In dual-helicopter suspended load missions, the UAH's flight speed is relatively slow; therefore, the aerodynamic forces on the fuselage are neglected, with only the rotor thrust considered, and both the magnitude and direction of the rotor thrust are adjustable.

Figure 1 is a schematic diagram of the DUH-SLS, and Figure 2 is its simplified diagram in the longitudinal plane.

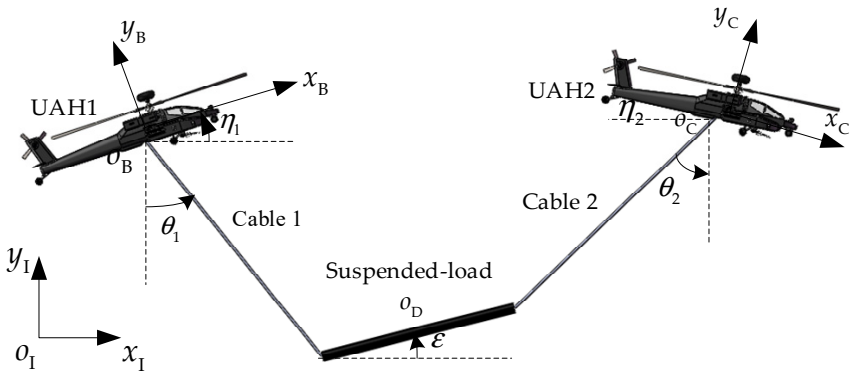


Figure 1. Schematic diagram of the DUH-SLS.

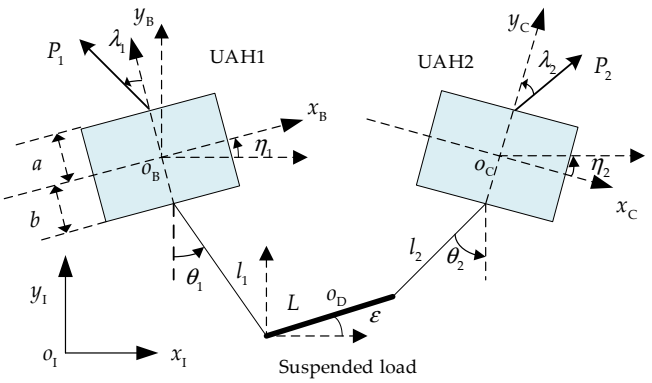


Figure 2. Simplified schematic diagram of the DUH-SLS.

The inertial coordinate system I ($o_I x_I y_I$), the UAH1 body-fixed coordinate system B ($o_B x_B y_B$), and the UAH2 body-fixed coordinate system C ($o_C x_C y_C$) are defined as illustrated in Figure 2. Table 2 provides the definitions and physical meanings of the symbols related to the DUH-SLS.

Table 2. Symbols and physical meanings of parameters in the DUH-SLS.

Parameter	Meaning
m_1, m_2, m_3	Mass of UAH1, UAH2, and the suspended load
I_1, I_2, I_3	Pitching moment of inertia of UAH1, UAH2, and the load
a, b	Geometric parameters of UAH1 and UAH2
L	Geometric length of the suspended load
l_1, l_2	Length of the sling cables 1 and 2
P_1, P_2	Rotor thrust of UAH1 and UAH2
λ_1, λ_2	Direction angle of the rotor thrust of UAH1 and UAH2
(x_s, y_s)	Coordinates of the centroid of the suspended load in the I-frame
η_1, η_2	Pitch angle of UAH1 and UAH2
ε	Pitch angle of the suspended load
θ_1, θ_2	Swing angle of the cables 1 and 2

Figure 3 is the motion constraint structure diagram of the DUH-SLS.

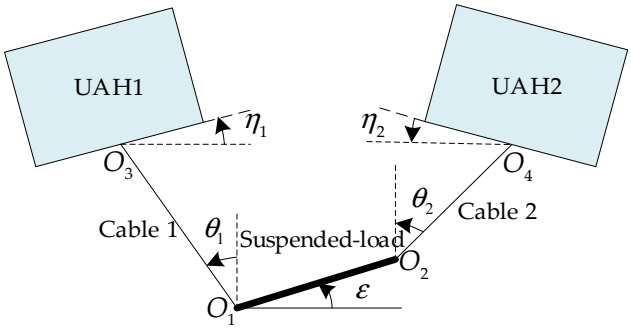


Figure 3. Motion constraint structure diagram for the DUH-SLS.

In Figure 3, $O_1 \sim O_4$ denote rotational joint constraints between each pair of connected rigid bodies (with the cables also regarded as rigid bodies without mass). Each rotational joint provides one rotational DOF. Starting from (but not including) the suspended load, the motion of each rigid body in this system can be regarded as a rotation relative to the preceding rigid body; thus, the system as a whole possesses four independent rotational DOFs. The suspended load itself has two translational DOFs for its centroid and one DOF for pitch motion. Thus, the DUH-SLS described herein possesses seven independent motion DOFs in total. Accordingly, a set of independent and complete generalized coordinates for the system is chosen as

$$q \triangleq [x_s, y_s, \varepsilon, \theta_1, \theta_2, \eta_1, \eta_2]^T \tag{1}$$

2.1. Dynamics Modeling

In Figure 2, o_B, o_C, o_D represent the centroids of UAH1, UAH2, and the suspended load, respectively. Their absolute position vectors in the I-frame are described using generalized coordinates, as shown in Equation (2a–c). The subscript "I" in the lower right corner of Equation (2a–c) indicates that these are the coordinate components of the corresponding vector in the I-frame. This will not be repeated in the following text. (In this context, the term "absolute vector" refers to the vector relative to the origin of the I-frame.)

$$\boldsymbol{r}_{o_B} = \begin{pmatrix} x_s - \frac{L}{2}\cos\varepsilon - l_1\sin\theta_1 - b\sin\eta_1 \\ y_s - \frac{L}{2}\sin\varepsilon + l_1\cos\theta_1 + b\cos\eta_1 \end{pmatrix}_I \tag{2a}$$

$$\boldsymbol{r}_{o_C} = \begin{pmatrix} x_s + \frac{L}{2}\cos\varepsilon - l_2\sin\theta_2 - b\sin\eta_2 \\ y_s + \frac{L}{2}\sin\varepsilon + l_2\cos\theta_2 + b\cos\eta_2 \end{pmatrix}_I \tag{2b}$$

$$\boldsymbol{r}_{o_D} = (x_s, y_s)_I^T \tag{2c}$$

Calculating the first-order time derivative of the absolute position vector in Equation (2a–c) yields the corresponding absolute velocity vectors $\boldsymbol{v}_{o_B}, \boldsymbol{v}_{o_C}, \boldsymbol{v}_{o_D}$. Similarly, the absolute angular velocity vectors of UAH1, UAH2, and the suspended load can be obtained as follows:

$$\boldsymbol{\omega}_{o_B} = \boldsymbol{a}_3\dot{\eta}_1 \tag{3a}$$

$$\boldsymbol{\omega}_{o_C} = \boldsymbol{a}_3\dot{\eta}_2 \tag{3b}$$

$$\boldsymbol{\omega}_{o_D} = \boldsymbol{a}_3\dot{\varepsilon} \tag{3c}$$

where $\boldsymbol{a}_3$ is the unit vector perpendicular to the coordinate plane of the I-frame outward.

In this paper, the dynamics model of the DUH-SLS is established using the second method of Lagrange analytical mechanics (Equation (4)).

$$\frac{\mathrm{d}}{\mathrm{d}t}\left(\frac{\partial L_{sys}}{\partial \dot{q}_i}\right) - \frac{\partial L_{sys}}{\partial q_i} = Q_i\ , (i = 1, 2, \cdots, 7) \tag{4}$$

In Equation (4), L_{sys} represents the Lagrange function, and it is defined as $L_{sys} = T - U$, where T denotes the kinetic energy of the system and U denotes the gravitational potential energy. (The local ground plane is regarded as the zero gravitational potential energy surface.) The expression of the L_{sys} is given by Equation (5).

$$\begin{aligned} L_{sys} &= \tfrac{1}{2}m_1\|\boldsymbol{v}_{o_B}\|^2 + \tfrac{1}{2}m_2\|\boldsymbol{v}_{o_C}\|^2 + \tfrac{1}{2}m_3\|\boldsymbol{v}_{o_D}\|^2 + \tfrac{1}{2}I_1\|\boldsymbol{\omega}_{o_B}\|^2 \\ &+ \tfrac{1}{2}I_2\|\boldsymbol{\omega}_{o_C}\|^2 + \tfrac{1}{2}I_3\|\boldsymbol{\omega}_{o_D}\|^2 - m_1 g(y_s - \tfrac{L}{2}\sin\varepsilon + l_1\cos\theta_1 + b\cos\eta_1) \\ &- m_2 g(y_s + \tfrac{L}{2}\sin\varepsilon + l_2\cos\theta_2 + b\cos\eta_2) - m_3 g y_s \end{aligned} \tag{5}$$

It is known that the main force P_1, P_2 on this system is the rotor thrust of UAH1 and UAH2. The position vector matrix of the P_1, P_2 acting point can be set as $\boldsymbol{r}_{sys} = [\boldsymbol{r}_{P_1}, \boldsymbol{r}_{P_2}]^T$, where

$$\begin{cases} \boldsymbol{r}_{P_1} = \begin{pmatrix} x_s - \frac{L}{2}\cos\varepsilon - l_1\sin\theta_1 - (a+b)\sin\eta_1 \\ y_s - \frac{L}{2}\sin\varepsilon + l_1\cos\theta_1 + (a+b)\cos\eta_1 \end{pmatrix}_I = \begin{pmatrix} \xi_1 \\ \xi_2 \end{pmatrix}_I \\ \boldsymbol{r}_{P_2} = \begin{pmatrix} x_s + \frac{L}{2}\cos\varepsilon - l_2\sin\theta_2 - (a+b)\sin\eta_2 \\ y_s + \frac{L}{2}\sin\varepsilon + l_2\cos\theta_2 + (a+b)\cos\eta_2 \end{pmatrix}_I = \begin{pmatrix} \xi_3 \\ \xi_4 \end{pmatrix}_I \end{cases} \tag{6}$$

The vector matrix of the main force acting on UAH1 and UAH2 is set as $\boldsymbol{F}_{sys} = [\boldsymbol{F}_1^{P_1}, \boldsymbol{F}_2^{P_2}]^T$, and its specific expressions are shown as follows:

$$\begin{cases} \boldsymbol{F}_1^{P_1} = [-P_1\sin(\lambda_1 + \eta_1), P_1\cos(\lambda_1 + \eta_1)]_I^T \\ \boldsymbol{F}_2^{P_2} = [-P_2\sin(\lambda_2 + \eta_2), P_2\cos(\lambda_2 + \eta_2)]_I^T \end{cases} \tag{7}$$

The formula for calculating the generalized forces is given by Equation (8).

$$Q_j = \sum_{i=1}^{2} \boldsymbol{F}_{\mathrm{sys}}(i) \cdot \frac{\partial[\boldsymbol{r}_{\mathrm{sys}}(i)]}{\partial q_j}\ ,\ (j = 1, 2, \cdots, 7) \tag{8}$$

We substitute Equations (6) and (7) into Equation (8) to obtain the expression of generalized forces as follows:

$$\begin{cases} Q_1 = -P_1 \sin(\eta_1 + \lambda_1) - P_2 \sin(\eta_2 + \lambda_2) \\ Q_2 = P_1 \cos(\eta_1 + \lambda_1) + P_2 \cos(\eta_2 + \lambda_2) \\ Q_3 = -\frac{L}{2} P_1 \cos(\eta_1 + \lambda_1 - \varepsilon) + \frac{L}{2} P_2 \cos(\eta_2 + \lambda_2 - \varepsilon) \\ Q_4 = P_1 l_1 \sin(\eta_1 + \lambda_1 - \theta_1) \\ Q_5 = P_2 l_2 \sin(\eta_2 + \lambda_2 - \theta_2) \\ Q_6 = (a+b) P_1 \sin\lambda_1, Q_7 = (a+b) P_2 \sin\lambda_2 \end{cases} \tag{9}$$

In summary, by combining Equations (4), (5) and (9), the dynamics equations of the DUH-SLS are derived as shown in Equation (10).

$$\begin{cases} (m_1+m_2+m_3)\ddot{x}_s - m_1 l_1 \cos\theta_1 \ddot{\theta}_1 - m_2 l_2 \cos\theta_2 \ddot{\theta}_2 - m_1 b \cos\eta_1 \ddot{\eta}_1 - m_2 b \cos\eta_2 \ddot{\eta}_2 + \frac{L}{2}\sin\varepsilon(m_1 - m_2)\ddot{\varepsilon} \\ +m_1(\frac{L}{2}\dot{\varepsilon}^2 \cos\varepsilon + l_1 \dot{\theta}_1^2 \sin\theta_1 + b\dot{\eta}_1^2 \sin\eta_1) + m_2(-\frac{L}{2}\dot{\varepsilon}^2 \cos\varepsilon + l_2 \dot{\theta}_2^2 \sin\theta_2 + b\dot{\eta}_2^2 \sin\eta_2) \\ +P_1 \sin(\eta_1 + \lambda_1) + P_2 \sin(\eta_2 + \lambda_2) = 0 \\ \\ (m_1+m_2+m_3)\ddot{y}_s - m_1 l_1 \sin\theta_1 \ddot{\theta}_1 - m_2 l_2 \sin\theta_2 \ddot{\theta}_2 - m_1 b \sin\eta_1 \ddot{\eta}_1 - m_2 b \sin\eta_2 \ddot{\eta}_2 + \frac{L}{2}\cos\varepsilon(m_2 - m_1)\ddot{\varepsilon} \\ -m_1(-\frac{L}{2}\dot{\varepsilon}^2 \sin\varepsilon + l_1 \dot{\theta}_1^2 \cos\theta_1 + b\dot{\eta}_1^2 \cos\eta_1) + m_2(-\frac{L}{2}\dot{\varepsilon}^2 \sin\varepsilon - l_2 \dot{\theta}_2^2 \sin\theta_2 - b\dot{\eta}_2^2 \sin\eta_2) \\ +(m_1+m_2+m_3)g - P_1 \cos(\eta_1 + \lambda_1) - P_2 \cos(\eta_2 + \lambda_2) = 0 \\ \\ -m_1 l_1 \cos\theta_1 \ddot{x}_s - m_1 l_1 \sin\theta_1 \ddot{y}_s + m_1 l_1^2 \ddot{\theta}_1 + m_1 b l_1 \cos(\eta_1 - \theta_1)\ddot{\eta}_1 + \frac{L}{2} m_1 l_1 \sin(\theta_1 - \varepsilon)\ddot{\varepsilon} \\ -\frac{L}{2} m_1 l_1 \dot{\varepsilon}^2 \cos(\theta_1 - \varepsilon) - m_1 b l_1 \sin(\eta_1 - \theta_1)\dot{\eta}_1^2 - m_1 g l_1 \sin\theta_1 - P_1 l_1 \sin(\eta_1 + \lambda_1 - \theta_1) = 0 \\ \\ -m_2 l_2 \cos\theta_2 \ddot{x}_s - m_2 l_2 \sin\theta_2 \ddot{y}_s + m_2 l_2^2 \ddot{\theta}_2 + m_2 b l_2 \cos(\eta_2 - \theta_2)\ddot{\eta}_2 - \frac{L}{2} m_2 l_2 \sin(\theta_2 - \varepsilon)\ddot{\varepsilon} \\ +\frac{L}{2} m_2 l_2 \dot{\varepsilon}^2 \cos(\theta_2 - \varepsilon) - m_2 b l_2 \sin(\eta_2 - \theta_2)\dot{\eta}_2^2 - m_2 g l_2 \sin\theta_2 - P_2 l_2 \sin(\eta_2 + \lambda_2 - \theta_2) = 0 \\ \\ -m_1 b \cos\eta_1 \ddot{x}_s - m_1 b \sin\eta_1 \ddot{y}_s + m_1 b l_1 \cos(\eta_1 - \theta_1)\ddot{\theta}_1 + (I_1 + m_1 b^2)\ddot{\eta}_1 + \frac{L}{2} m_1 b \sin(\eta_1 - \varepsilon)\ddot{\varepsilon} \\ -\frac{L}{2} m_1 b \dot{\varepsilon}^2 \cos(\eta_1 - \varepsilon) + m_1 b l_1 \sin(\eta_1 - \theta_1)\dot{\theta}_1^2 - m_1 g b \sin\eta_1 - (a+b) P_1 \sin\lambda_1 = 0 \\ \\ -m_2 b \cos\eta_2 \ddot{x}_s - m_2 b \sin\eta_2 \ddot{y}_s + m_2 b l_2 \cos(\eta_2 - \theta_2)\ddot{\theta}_2 + (I_2 + m_2 b^2)\ddot{\eta}_2 - \frac{L}{2} m_2 b \sin(\eta_2 - \varepsilon)\ddot{\varepsilon} \\ +\frac{L}{2} m_2 b \cos(\eta_2 - \varepsilon)\dot{\varepsilon}^2 + m_2 b l_2 \sin(\eta_2 - \theta_2)\dot{\theta}_2^2 - m_2 g b \sin\eta_2 - (a+b) P_2 \sin\lambda_2 = 0 \\ \\ \frac{L}{2}(m_1 - m_2)\sin\varepsilon \ddot{x}_s + \frac{L}{2}(m_2 - m_1)\cos\varepsilon \ddot{y}_s + \frac{L}{2} m_1 l_1 \sin(\theta_1 - \varepsilon)\ddot{\theta}_1 - \frac{L}{2} m_2 l_2 \sin(\theta_2 - \varepsilon)\ddot{\theta}_2 \\ +\frac{L}{2} m_1 b \sin(\eta_1 - \varepsilon)\ddot{\eta}_1 - \frac{L}{2} m_2 b \sin(\eta_2 - \varepsilon)\ddot{\eta}_2 + (\frac{L^2}{4} m_1 + \frac{L^2}{4} m_2 + I_3)\ddot{\varepsilon} + \frac{L}{2} m_1 l_1 \cos(\theta_1 - \varepsilon)\dot{\theta}_1^2 \\ +\frac{L}{2} m_1 b \cos(\eta_1 - \varepsilon)\dot{\eta}_1^2 - \frac{L}{2} m_2 l_2 \cos(\theta_2 - \varepsilon)\dot{\theta}_2^2 - \frac{L}{2} m_2 b \cos(\eta_2 - \varepsilon)\dot{\eta}_2^2 - \frac{L}{2} m_1 g \cos\varepsilon \\ +\frac{L}{2} m_2 g \cos\varepsilon + \frac{L}{2} P_1 \cos(\eta_1 + \lambda_1 - \varepsilon) - \frac{L}{2} P_2 \cos(\eta_2 + \lambda_2 - \varepsilon) = 0 \end{cases} \tag{10}$$

After mathematical transformation, the above equation can be written as the general form of the dynamics equation $M\ddot{q} = h(q, \dot{q})$, where M is the mass/inertia matrix of the DUH-SLS. Define the state vector and control vector of the DUH-SLS, as shown in Equation (11). It can be seen from these equations that the system possesses four control variables against seven independent degrees of freedom, making it a typical underactuated system.

$$\begin{cases} X = (q^{\mathrm{T}}, \dot{q}^{\mathrm{T}})^{\mathrm{T}},\ u = (P_1, P_2, \lambda_1, \lambda_2)^{\mathrm{T}} \end{cases} \tag{11}$$

$h(q, \dot{q})$ explicitly contains control variables and can, therefore, be further written as $h(q, \dot{q}, u)$. Thus, the state-space representation of the DUH-SLS can be expressed as Equation (12).

$$\dot{X} = \begin{pmatrix} 0_{7\times7} & I_{7\times7} \\ 0_{7\times7} & 0_{7\times7} \end{pmatrix} \begin{pmatrix} q \\ \dot{q} \end{pmatrix} + \begin{pmatrix} 0_{7\times1} \\ M^{-1}h(q, \dot{q}, u) \end{pmatrix} \triangleq F(X, u) \tag{12}$$

The aforementioned state-space representation provides convenience for controller design using modern control theory and for conducting numerical simulations of the system's dynamic processes.

2.2. Correctness Verification of the Dynamics Model of DUH-SLS

To verify the correctness of the dynamics model of the DUH-SLS established in the last section, a virtual prototype of this system is built using ADAMS software in this section, and numerical simulations are carried out. The model parameters of the DUH-SLS are set as shown in Table 3.

Table 3. The model parameter values of DUH-SLS.

Model Parameter/Unit	Value	Model Parameter/Unit	Value
$m_1, m_2/\mathrm{kg}$	400	a/m	3
m_3/kg	300	b/m	2
$I_1, I_2/\mathrm{kg \cdot m^2}$	250	L/m	5
$I_3/\mathrm{kg \cdot m^2}$	200	$l_1, l_2/\mathrm{m}$	12

A virtual prototype of the DUH-SLS is established in ADMAS software (ADAMS View 2018), with a schematic diagram shown in Figure 4.

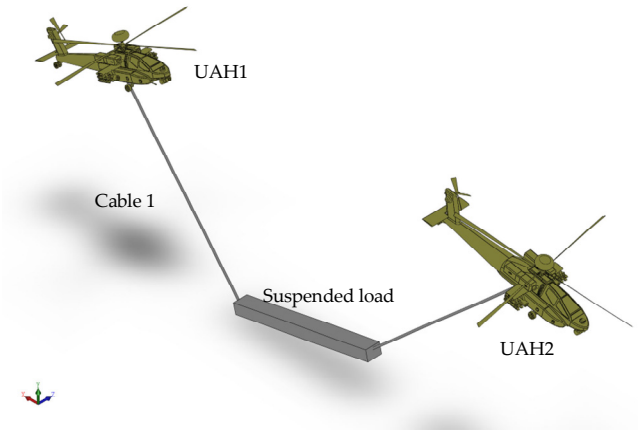


Figure 4. Schematic diagram of the DUH-SLS's virtual prototype.

A self-developed MATLAB (MATLAB R2024b) program based on the fourth-order Runge–Kutta algorithm was used to numerically solve the dynamics differential equations of the DUH-SLS shown in Equation (10), thereby obtaining the system's motion state response curves. Meanwhile, under identical working conditions, dynamics simulation of the virtual prototype was conducted using ADAMS software to acquire the corresponding state response curves. The state response curves obtained by both methods are shown in Figure 5.

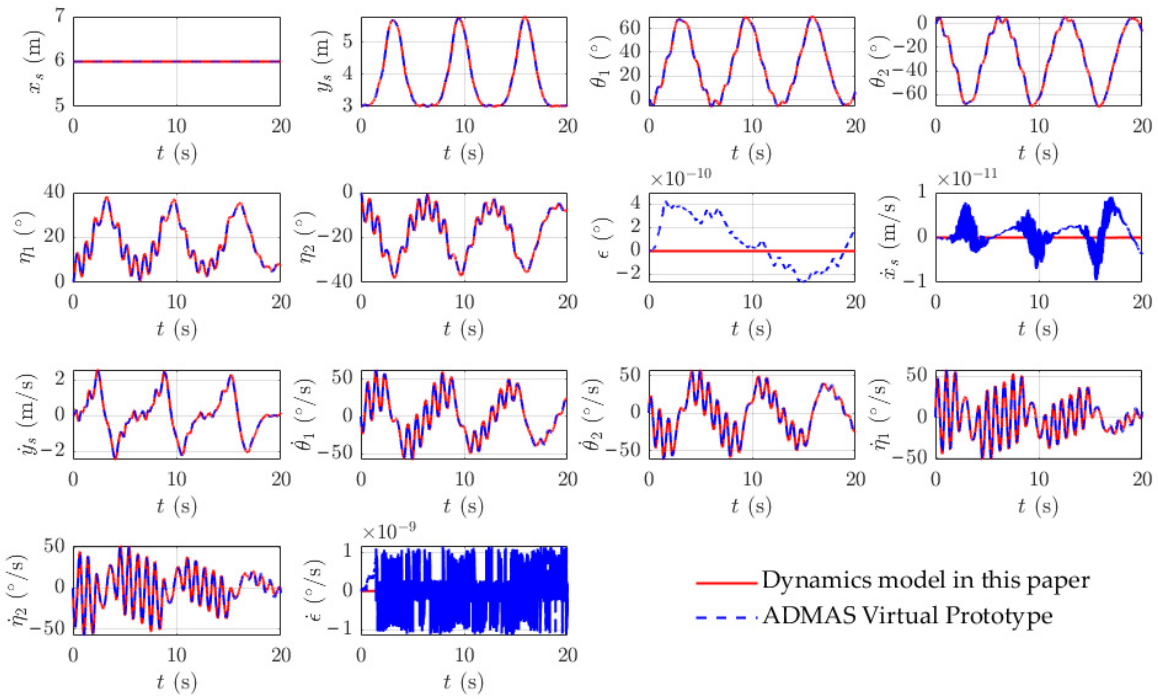


Figure 5. Comparison of state variables over time between the theoretical model and the virtual prototype under identical simulation conditions.

The simulation results in Figure 5 show that the state variables from the two approaches exhibit good overall agreement in terms of response trends and amplitudes, indicating that the established nonlinear dynamics theoretical model can effectively reflect the system's dynamic characteristics and verifying the correctness of the DUH-SLS nonlinear dynamics theoretical model established in this paper. Minor discrepancies are observed in some state variables, such as the suspended load's pitch angle and pitch angular velocity, which are on the order of 10^{-9} and can be attributed to the integration accuracy of the numerical integration method, rendering them negligible. Overall, the theoretical model demonstrates high accuracy and reliability, and it provides a reliable theoretical basis for system stability analysis and control strategy design.

3. Design of Cooperative Controller for DUH-SLS

This section aims to design an integrated optimal controller for the underactuated DUH-SLS capable of achieving simultaneous trajectory tracking and suspended load swing suppression. To this end, the iterative Linear Quadratic Regulator (iLQR) method is employed. The section first formulates a nonlinear quadratic optimal control problem for the DUH-SLS, subsequently details the complete procedure for solving this problem using the iLQR algorithm, and finally presents the mathematical form of the controller along with its characteristic analysis.

3.1. Problem Formulation: Integrated Trajectory Tracking and Swing Suppression Control

The state-space representation of the DUH-SLS (Equation (12)) is first discretized into the nonlinear difference equation:

$$\begin{aligned} X_{k+1} &= X_k + F(X_k, u_k) \cdot T_s \triangleq F_{\mathrm{d}}(X_k, u_k) \\ &= X_k + T_s \cdot \left\{ \begin{pmatrix} 0_{7\times7} & I_{7\times7} \\ 0_{7\times7} & 0_{7\times7} \end{pmatrix} \begin{pmatrix} q_k \\ \dot{q}_k \end{pmatrix} + \begin{pmatrix} 0_{7\times1} \\ M^{-1}h(q_k, \dot{q}_k, u_k) \end{pmatrix} \right\} \end{aligned} \tag{13}$$

where "F_d" denotes the state transition function of the discretized system, and T_s represents the sampling time (or the discrete-time step). The state vector and control vector at time step k are defined as

$$\begin{cases} X_k = (x_{sk}, y_{sk}, \varepsilon_k, \theta_{1k}, \theta_{2k}, \eta_{1k}, \eta_{2k}, \dot{x}_{sk}, \dot{y}_{sk}, \dot{\varepsilon}_k, \dot{\theta}_{1k}, \dot{\theta}_{2k}, \dot{\eta}_{1k}, \dot{\eta}_{2k})^{\mathrm{T}}, (k = 1 \sim n+1) \\ u_k = (P_{1k}, P_{2k}, \lambda_{1k}, \lambda_{2k})^{\mathrm{T}}, (k = 1 \sim n) \end{cases} \tag{14}$$

In Section 2.1, the centroid coordinates of UAH1 and UAH2 are not directly used as generalized coordinates; instead, their centroids are described by the selected set of generalized coordinates, as shown in Equation (2a–c). Therefore, trajectory tracking for the DUH-SLS can be equivalently formulated as tracking the position trajectory of the suspended load's centroid. Therefore, the control objectives are twofold: (1) accurate tracking of a predefined reference trajectory $(x_{sk}^{\mathrm{c}}, y_{sk}^{\mathrm{c}})^{\mathrm{T}}$ $(k = 1 \sim n+1)$ (denoted by the superscript "c") for the suspended load's centroid, and (2) effective suppression of its swing angles θ_1 and θ_2. The DUH-SLS is an underactuated system, meaning the number of control inputs is fewer than the generalized coordinates. Consequently, when the suspended load's centroid position and swing angles are regulated to their desired values, the remaining states converge to values satisfying the system's force and moment equilibrium. The output command sequence is thus defined as $y_k = CX_k^{\mathrm{c}} = (x_{sk}^{\mathrm{c}}, y_{sk}^{\mathrm{c}}, \theta_{1k}^{\mathrm{c}}, \theta_{2k}^{\mathrm{c}})^{\mathrm{T}} (k = 1 \sim n+1)$, where C is the output matrix.

Synthesizing these objectives, the integrated optimal control problem for the DUH-SLS is formulated as minimizing a quadratic cost function subject to the system's dynamics difference equations:

$$\begin{cases} \min J = \frac{1}{2}(X_{n+1} - X_{n+1}^{\mathrm{c}})^{\mathrm{T}} F (X_{n+1} - X_{n+1}^{\mathrm{c}}) \\ \quad + \frac{1}{2} \sum_{k=1}^{n} [(X_k - X_k^{\mathrm{c}})^{\mathrm{T}} Q (X_k - X_k^{\mathrm{c}}) + u_k{}^{\mathrm{T}} R u_k] \\ \text{s.t.} \begin{cases} X_{k+1} = F_d(X_k, u_k) \\ X_1 = \hat{X}_1 \end{cases} \end{cases} \tag{15}$$

Here, $Q, F \in \mathbb{R}^{14\times14}$ are positive semi-definite state weighting matrices; $R \in \mathbb{R}^{4\times4}$ is a positive definite control weighting matrix; and X_k^{c} is the extended state command vector incorporating both the load's centroid reference trajectory and desired swing angles.

3.2. iLQR Solution Framework and Nonlinear Optimal Controller Design

The problem described in Equation (15) represents a nonlinear optimal control problem with a quadratic performance index, which cannot be solved directly using the linear-quadratic (LQ) theory. However, the iLQR method addresses this by performing pointwise linearization of the system dynamics around a nominal state and control trajectory, thereby transforming the original nonlinear problem into a sequence of LQR subproblems. This approach combines linearization with an iterative optimization strategy to successively approximate the solution to the original nonlinear optimal control problem. The following steps describe how to apply the iLQR method to the DUH-SLS system.

Step 1: Initialization. An initial nominal control sequence $\{u_k^*\}$ $(k = 1 \sim n)$ is (e.g., a zero-control sequence $\{0_k\}$ $(k = 1 \sim n)$), By substituting the initial control sequence into the state difference equation described in Equation (13) and using the value of the initial state $(\hat{X}_1)$, the corresponding nominal state sequence $\{X_k^*\}$ $(k = 1 \sim n+1)$ can be obtained through forward iteration along the time axis.

Step 2: Sequential Linearization. At the nominal trajectory $\{X_k^*\}\{u_k^*\}$ $(k = 1 \sim n)$ obtained from the current iteration (or provided initially), a first-order Taylor expansion is

applied to the system's nonlinear state equations (Equation (13)), yielding a locally linear difference equation shown as follows.

$$\delta X_{k+1} = A_k \delta X_k + B_k \delta u_k \tag{16}$$

where

$$\begin{cases} \delta X_k = X_k - X_k^* \\ \delta u_k = u_k - u_k^* \end{cases} \tag{17}$$

$$A_k = \left.\frac{\partial F_d}{\partial X}\right|_{\substack{X = X_k^* \\ u = u_k^*}}, \; B_k = \left.\frac{\partial F_d}{\partial u}\right|_{\substack{X = X_k^* \\ u = u_k^*}} \tag{18}$$

The matrices A_k and B_k are the state and control Jacobians, respectively, calculated along the nominal state and control trajectory. Among Equations (16) and (17), there are $A_k \in \mathbb{R}^{14\times 14}$, $B_k \in \mathbb{R}^{14\times 4}$.

Step 3: LQR Subproblem Solution. Based on the linearized dynamics (16) and the quadratic cost function from Equation (15), a local Linear Quadratic Regulator (LQR) problem is formulated in Equation (19).

$$\begin{cases} \min J = \frac{1}{2}(X_{n+1}^* + \delta X_{n+1} - X_{n+1}^c)^T F (X_{n+1}^* + \delta X_{n+1} - X_{n+1}^c) + \\ \frac{1}{2}\sum_{i=1}^{n} \left[(X_k^* + \delta X_k - X_{k+1}^c)^T Q (X_k^* + \delta X_k - X_{k+1}^c) + (u_k^* + \delta u_k)^T R (u_k^* + \delta u_k)\right] \\ \text{s.t.} \begin{cases} \delta X_{k+1} = A_k \delta X_k + B_k \delta u_k \\ \delta X_1 = 0 \end{cases} \end{cases} \tag{19}$$

where $\{X_k^*\}\,(k = 1 \sim n+1)$ and $\{u_k^*\}\,(k = 1 \sim n)$ denote the state sequence and control sequence generated from the previous iteration, respectively, which correspond to the initially given values during the first iteration. $\{X_k^c\}\,(k = 1 \sim n)$ represents the desired reference trajectory, where the superscript "c" indicates the reference command. The expression $X_k^* + \delta X_k - X_{k+1}^c$ represents the tracking error of the updated trajectory relative to the reference trajectory. The physical quantities to be optimized in the above problem are the correction terms of the control sequence $\{\delta u_k\}\,(k = 1 \sim n)$.

According to the variational method and Pontryagin's minimum principle, the solution to this subproblem provides the optimal control correction $\{\delta u_k\}\,(k = 1 \sim n)$ in a feedback form:

$$\delta u_k = -K_k \delta X_k - K_{v,k} v_{k+1} - K_{u,k} u_k^* \tag{20}$$

where the time-varying gain matrices $K_k, K_{v,k}, K_{u,k}$ are computed as

$$\begin{cases} K_k = -(B_k^T S_{k+1} B_k + R)^{-1} B_k^T S_{k+1} A_k \\ K_{v,k} = (B_k^T S_{k+1} B_k + R)^{-1} B_k^T \\ K_{u,k} = (B_k^T S_{k+1} B_k + R)^{-1} R \end{cases} \tag{21}$$

The matrix sequence $\{S_k\}\,(k = 2 \sim n+1)$ and vector sequence $\{v_k\}\,(k = 2 \sim n+1)$ are obtained through backward-in-time recursion, starting from the terminal conditions

$$\begin{cases} S_k = A_k^T S_{k+1}(A_k - B_k K) + Q \\ v_k = (A_k - B_k K)^T v_{k+1} - K^T R u_k + Q(X_k^* + \delta X_k - X_k^c) \\ S_{n+1} = F, v_{n+1} = F \cdot (X_{n+1}^* + \delta X_{n+1} - X_{n+1}^c) \end{cases} \tag{22}$$
$(k = 2 \sim n)$

Step 4: Forward Calculate and Update. The initial correction of the state sequence is always zero, i.e., $\delta X_1 = 0$. According to Equation (20), the corresponding control correction δu_1 can be calculated. Substituting this into Equation (16), the state correction $\delta X_2 = 0$ at the next time step is propagated forward along the time axis. Repeating this process until the complete correction sequences of the state and control sequences, $\{\delta X_k\}\,(k = 1 \sim n+1)$ and $\{\delta u_k\}\,(k = 1 \sim n)$, are computed. Finally, the state and control sequences are updated based on the obtained corrections, with the updated formulas given as follows:

$$\begin{cases} X_k^{\text{new}} = X_k^* + \delta X_k \\ u_k^{\text{new}} = u_k^* + \delta u_k \end{cases} \tag{23}$$

Step 5: Convergence Check. The performance index J^{new} of the updated trajectory is calculated. If the reduction in its value relative to the previous iteration is less than a prespecified threshold, the iteration terminates. Otherwise, the updated trajectory $\left\{X_k^{\text{new}}, u_k^{\text{new}}\right\}\,(k = 1 \sim n)$ is set as the new nominal trajectory $\left\{X_k^*, u_k^*\right\}\,(k = 1 \sim n)$, and the process returns to **Step 2** for the next iteration.

The offline iLQR iteration converges to an optimal nominal control sequence $\left\{u_k^{\text{opt}}\right\}\,(k = 1 \sim n)$ and its corresponding state trajectory $\left\{X_k^{\text{opt}}\right\}\,(k = 1 \sim n+1)$. For online implementation, these are treated as the reference trajectories $\left\{X_k^*, u_k^*\right\}\,(k = 1 \sim n)$.

A key advantage of the iLQR controller is that the update law (Equations (20) and (23)) inherently provides a state-feedback form. During online operation, if the measured state X_k deviates from the predefined nominal state X_k^*, the state error $\delta X_k = X_k - X_k^*$ is fed into the precomputed feedback control law.

$$\delta u_k = -K_k \delta X_k - K_{v,k} v_{k+1} - K_{u,k} u_k^{\text{opt}} \tag{24}$$

The final control command applied to the system is

$$u_k = u_k^{\text{opt}} + \delta u_k \tag{25}$$

This constitutes a closed-loop control strategy. Therefore, the iLQR-based controller not only addresses the nonlinear optimal control design challenge but also incorporates inherent feedback, granting the system a certain robustness against model uncertainties and external disturbances. This controller is hereafter referred to as the iLQR optimal controller.

3.3. Design of Controllers for Comparison

To demonstrate the performance advantages of the controller designed in Section 3.2, this section presents the design of both an LQR optimal controller and an LMC nonlinear controller for the DUH-SLS. Due to space limitations, only the important expressions for these two controllers are provided here, with additional detailed formulas available in Appendix A.

LQR optimal controller:

Firstly, the state equation of the DUH-SLS described by Equation (12) is discretized into a state difference equation and then linearized around an equilibrium point $\left\{X_k^{\text{c}}, u^*\right\}$ via small perturbations, resulting in the following linearized state difference equation (u^* represents the value of control variables of DUH-SLS at the equilibrium point).

$$\begin{cases} \Delta X_{k+1} = \widetilde{A}_{\text{L}} \Delta X_k + \widetilde{B}_{\text{L}} \Delta u_k \\ \Delta X_k = X_k - X_i^{\text{c}} \\ \Delta u_k = u_k - u^* \end{cases} \tag{26}$$

where

$$\widetilde{A}_{\mathrm{L}} = \left.\frac{\partial F_{\mathrm{d}}}{\partial X}\right|_{\substack{X = X_k^{\mathrm{c}} \\ u = u^*}}, \quad \widetilde{B}_{\mathrm{L}} = \left.\frac{\partial F_{\mathrm{d}}}{\partial u}\right|_{\substack{X = X_k^{\mathrm{c}} \\ u = u^*}} \tag{27}$$

By designing a quadratic performance index for the linear controlled system described above, an LQR problem can be obtained. The resulting integrated LQR optimal controller for trajectory tracking and swing suppression of the DUH-SLS is given as follows:

$$\begin{cases} P_k = Q + \widetilde{A}_L^T P_{k+1}(I + \widetilde{B}_{\mathrm{L}} R^{-1} \widetilde{B}_{\mathrm{L}}^{\mathrm{T}} P_{k+1})^{-1} \widetilde{A}_{\mathrm{L}}, \ (k = 2 \sim n) \\ g_k = \widetilde{A}_{\mathrm{L}}^{\mathrm{T}}[I - (I + \widetilde{B}_{\mathrm{L}} R^{-1} \widetilde{B}_{\mathrm{L}}^{\mathrm{T}} P_{k+1})^{-1} \widetilde{B}_{\mathrm{L}} R^{-1} \widetilde{B}_{\mathrm{L}}^{\mathrm{T}}] g_{k+1} - Q X_k^{\mathrm{c}}, \ (k = 2 \sim n) \\ P_{n+1} = F \\ g_{n+1} = -F X_{n+1}^{\mathrm{c}} \\ u_k = -(R + \widetilde{B}_{\mathrm{L}}^{\mathrm{T}} P_k \widetilde{B}_{\mathrm{L}})^{-1} \widetilde{B}_{\mathrm{L}}^{\mathrm{T}} P_k \widetilde{A}_{\mathrm{L}} \Delta X_k - (R + \widetilde{B}_{\mathrm{L}}^{\mathrm{T}} P_k \widetilde{B}_{\mathrm{L}})^{-1} \widetilde{B}_{\mathrm{L}}^{\mathrm{T}} g_{k+1} + u^*, \ (k = 1 \sim n) \end{cases} \tag{28}$$

LMC nonlinear controller:

According to Lyapunov stability theory, a positive definite Lyapunov energy function ($V = T + V_1 + V_2$) is first constructed. Where T denotes the kinetic energy of the system and V_1 represents the relative gravitational potential energy, which is always positive. V_2 is a constructive virtual energy function and its detailed expression is as follows:

$$\begin{aligned} V_2 = {} & \frac{1}{2}\sum_{i=1}^{4} k_i(\xi_i - \xi_i^{\mathrm{c}})^2 + (m_1 + \frac{1}{2}m_3)g[l_1(1 - \cos\theta_1) + (a+b)(1 - \cos\eta_1) \\ & + \frac{L}{2}(1 - \sin\varepsilon)] + (m_2 + \frac{1}{2}m_3)g[l_2(1 - \cos\theta_2) + (a+b)(1 - \cos\eta_2) \\ & + \frac{L}{2}(1 + \sin\varepsilon)], \ (i = 1 \sim 4) \end{aligned} \tag{29}$$

Based on Lyapunov stability theory, by defining $\dot{V} < 0$, which is shown in Equation (30), the integrated nonlinear controller for trajectory tracking and swing suppression of the DUH-SLS can be derived as Equation (31).

$$\dot{V} = -C_1\dot{\xi}_1^2 - C_2\dot{\xi}_2^2 - C_3\dot{\xi}_3^2 - C_4\dot{\xi}_3^4 - -C_5\dot{\xi}_4^2 - C_6\dot{\xi}_4^4 < 0 \tag{30}$$

$$\begin{cases} P_1 = \sqrt{(w_1^2 + w_3^2)} \\ \lambda_1 = \arctan(\frac{-w_1}{w_3}) - \eta_1 \end{cases}, \quad \begin{cases} P_2 = \sqrt{(w_2^2 + w_4^2)} \\ \lambda_2 = \arctan(\frac{-w_2}{w_4}) - \eta_2 \end{cases} \tag{31}$$

where

$$\begin{cases} w_1 = -k_1(\xi_1 - \xi_1^{\mathrm{c}}) - C_1\dot{\xi}_1, w_2 = -k_2(\xi_2 - \xi_2^{\mathrm{c}}) - C_2\dot{\xi}_2 \\ w_3 = (m_1 + \frac{1}{2}m_3)g - k_3(\xi_3 - \xi_3^{\mathrm{c}}) - C_3\dot{\xi}_3 - C_4(\dot{\xi}_3)^3 \\ w_4 = (m_2 + \frac{1}{2}m_3)g - k_4(\xi_4 - \xi_4^{\mathrm{c}}) - C_5\dot{\xi}_4 - C_6(\dot{\xi}_4)^3 \end{cases} \tag{32}$$

The relevant expressions for $\xi_1 \sim \xi_4$ are given in Equation (6). In Equations (30) and (32), $k_i(i = 1 \sim 4), C_j(j = 1 \sim 6)$ denote the undetermined-parameters undetermined parameters, which are strictly positive.

To improve the convergence efficiency of the iLQR offline iterative optimization, the simulation results of the LQR controller are employed as the initial guess for the state and control trajectories, providing a high-quality starting point for the iterative optimization process. Subsequent numerical simulation results demonstrate that this initialization strategy effectively accelerates convergence, enabling the iLQR to achieve convergence after only a single iteration, which exhibits remarkable computational efficiency. The schematic block diagram of the iLQR simulation principle is presented in Figure 6, while

the overall control block diagram of the DUH-SLS cooperative control system is shown in Figure 7.

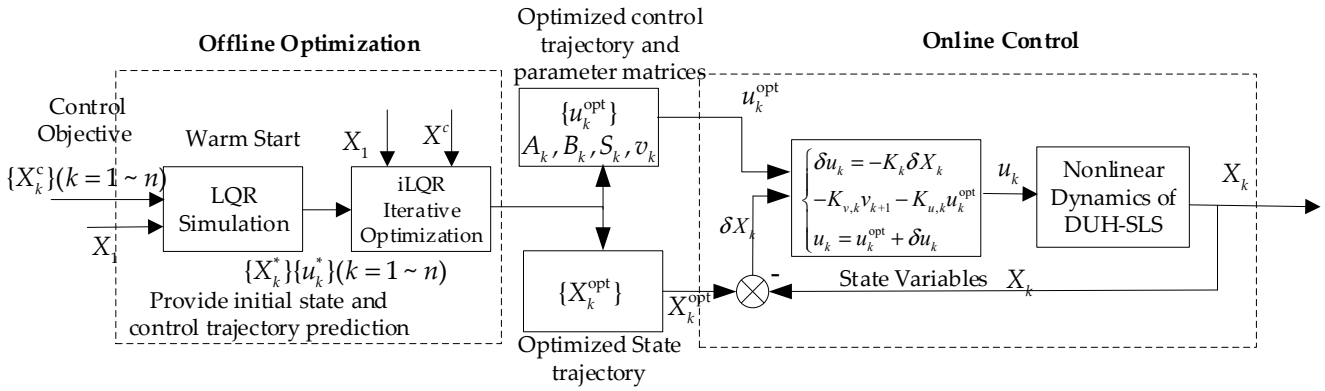


Figure 6. The schematic block diagram of the iLQR optimal controller.

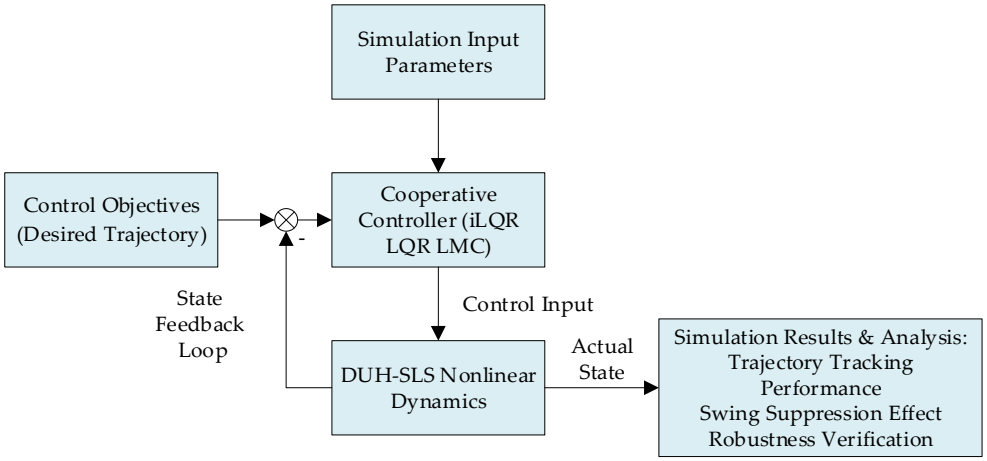


Figure 7. Control block diagram of the DUH-SLS cooperative control system.

4. Numerical Simulation

To evaluate the performance of the iLQR optimal controller designed in Section 3.2, numerical simulations of the DUH-SLS are conducted under two different task scenarios. The simulation task scenarios are defined as follows:

(1) Task Scenario 1: Hovering Control. In this task, the DUH-SLS is required to be precisely controlled to the commanded position and maintained at this position, while suppressing the swing of the suspended load and ensuring that the swing angles converge to the commanded values.

(2) Task Scenario 2: Trajectory Tracking. In this task, the DUH-SLS is required to accurately track a predefined reference trajectory, while suppressing the swing of the suspended load and ensuring that its pitch angle asymptotically converges to the specific value during this process.

The numerical simulations in this study are performed on a computing platform equipped with an AMD Ryzen 7 7840H CPU and 16 GB of RAM (purchased from Lenovo, Nanjing, China). This hardware configuration provides a stable computational environment, thereby ensuring the reliability and reproducibility of the simulation results.

4.1. Task Scenario 1: Hovering Control

The simulation input parameters are shown in Tables 3 and 4.

Table 4. Hovering Control: Simulation input parameters.

Parameter/Unit	Value	Parameter/Unit	Value
$(x_{s0}, y_{s0})/\mathrm{m}$	(5, 10)	$g/\mathrm{m}\cdot\mathrm{s}^{-2}$	9.8
$\theta_{10}/^\circ$	10	$P_{1\max}, P_{2\max}/N$	6500
$\theta_{20}/^\circ$	-10	$P_{1\min}, P_{2\min}/N$	0
$\eta_{10}/^\circ$	5	$\lambda_{1\max}, \lambda_{2\max}/^\circ$	25
$\eta_{20}/^\circ$	-5	$\lambda_{1\min}, \lambda_{2\min}/^\circ$	-25
$\varepsilon_0/^\circ$	10		

In Table 4, "$x_{s1}, y_{s1}, \varepsilon_1, \theta_{11}, \theta_{21}, \eta_{11}, \eta_{21}$" denotes the initial values of the state variable for the DUH-SLS, while "$P_{1\max}, P_{2\max}, P_{1\min}, P_{2\min}, \lambda_{1\max}, \lambda_{2\max}, \lambda_{1\min}, \lambda_{2\min}$" represents the range of the control variables. The command values of extended state variables at the hovering point are set as follows:

$$\begin{aligned} X^{\mathrm{c}} &= \left(x_{\mathrm{s}}^{\mathrm{c}}, y_{\mathrm{s}}^{\mathrm{c}}, \varepsilon^{\mathrm{c}}, \theta_1^{\mathrm{c}}, \theta_2^{\mathrm{c}}, \eta_1^{\mathrm{c}}, \eta_2^{\mathrm{c}}, \dot{x}_{\mathrm{s}}^{\mathrm{c}}, \dot{y}_{\mathrm{s}}^{\mathrm{c}}, \dot{\varepsilon}^{\mathrm{c}}, \dot{\theta}_1^{\mathrm{c}}, \dot{\theta}_2^{\mathrm{c}}, \dot{\eta}_1^{\mathrm{c}}, \dot{\eta}_2^{\mathrm{c}}\right)^{\mathrm{T}} \\ &= (15\mathrm{m}, 5\mathrm{m}, 0, 0, 0, 0, 0, 0, 0, 0, 0, 0, 0, 0)^{\mathrm{T}} \end{aligned} \tag{33}$$

The weighting matrix parameters for the iLQR optimal controller are determined through numerical simulation. Specifically, a trial-and-error approach combined with system response characteristics is adopted, and multiple simulation experiments are conducted to gradually adjust the Q and R matrices until a desirable balance between trajectory tracking accuracy and swing suppression performance is achieved. The final weighting matrix values, which represent the optimal parameter combination selected through comparative simulations, are given as follows:

$$\begin{cases} R = \mathrm{diag}(0.01;\ 0.01; 0.001; 0.001) \\ Q = \mathrm{diag}(102;\ 305;\ 510;\ 510;\ 8200; 8200; 8200; \\ 250;\ 500;\ 5100; 5150; 5000; 5000; 5000) \end{cases} \tag{34}$$

Figures 8 and 9 compare the performance of the three controllers based on the state response curves of the DUH-SLS, where the curves under the iLQR optimal controller are obtained after multiple iterations and convergence. Table 5 presents the peak values (defined as κ) of the two swing angles and the pitch angles of UAH1 and UAH2 during the last significant oscillation before convergence, as well as the peak values (defined as u_σ) of the control variables for UAH1 and UAH2.

Table 5. κ and u_σ under different controllers.

Parameters	State Variables	iLQR	LQR	LMC
κ	θ_1	4.4°	7.7°	9.7°
	θ_2	1.2°	5.1°	6.7°
	η_1	2.6°	4.3°	4.8°
	η_2	1.4°	3.2°	3.9°
u_σ	P_1	5589 N	5585 N	5528 N
	λ_1	-4°	-8°	-20°
	P_2	5862 N	5673 N	6426 N
	λ_1	1.5°	1.7°	-5.2°

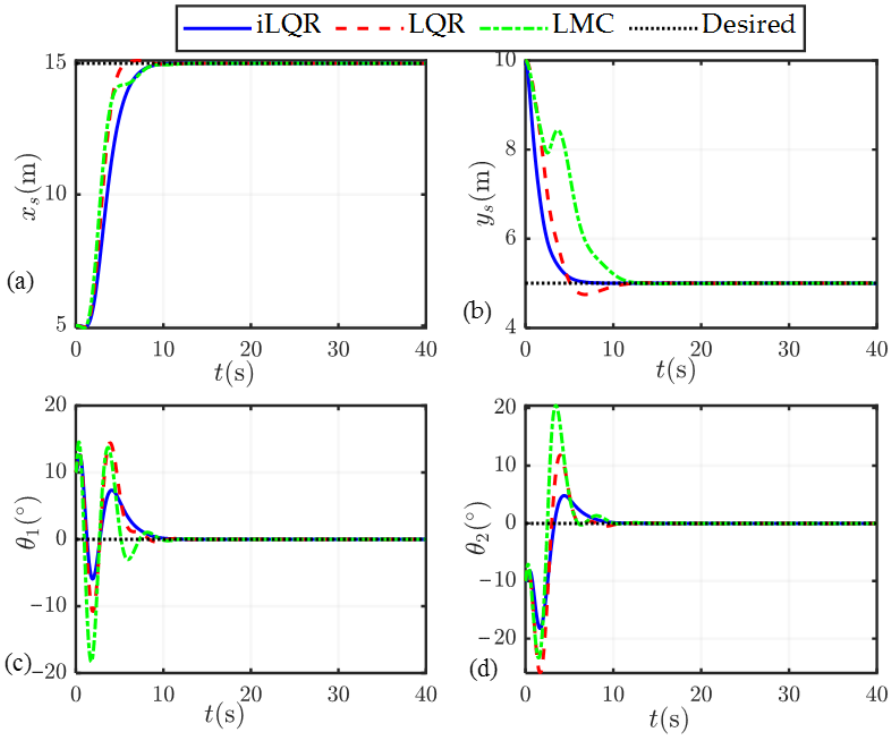


Figure 8. State response curves (position and swing angles) of the DUH-SLS under different controllers. (**a**) Variation curves of the X-coordinate of the suspended load's centroid; (**b**) variation curves of the Y-coordinate of the suspended load's centroid; (**c**) the curves of the swing angle of cable 1; (**d**) the curves of the swing angle of cable 2.

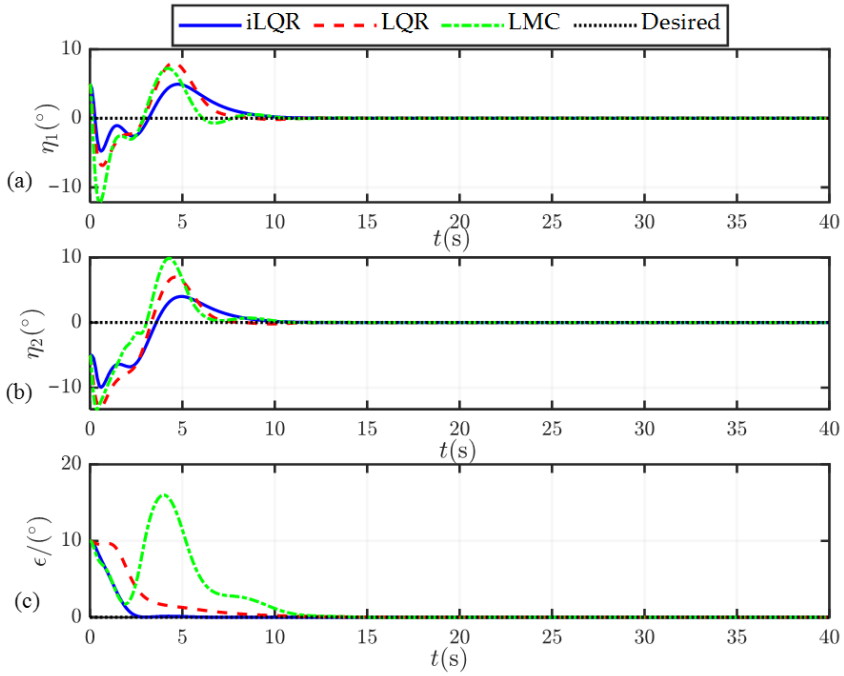


Figure 9. State response curves (pitch angles) of the DUH-SLS under different controllers. (**a**) Variation curves of UAH1's pitch angle; (**b**) variation curves of UAH2's pitch angle; (**c**) variation curves of the suspended load's pitch angle.

As shown in Figure 8, all three controllers enable the suspended load to rapidly reach the desired command position. However, under the iLQR optimal controller, the position curves exhibit smoother transitions without overshoot, and the oscillation amplitude of the swing angles is smaller, allowing the system to stably approach the desired position and

thereby enhancing the safety and reliability in hovering. Figure 9 indicated that, although the pitch angles of UAH1 and UAH2 converge slightly more slowly under the iLQR optimal controller, their oscillation amplitudes are smaller and the transitions are smoother, while the pitch angle of the suspended load converges rapidly and smoothly. Overall, the state curves demonstrate superior dynamic performance (smaller overshoot, lower oscillation peaks, and shorter settling time) under the iLQR optimal controller compared to the other two controllers. The simulation results in Table 5 further illustrate the superior performance of the iLQR optimal controller.

Figure 10 shows the variation curves of the control variables for the DUH-SLS.

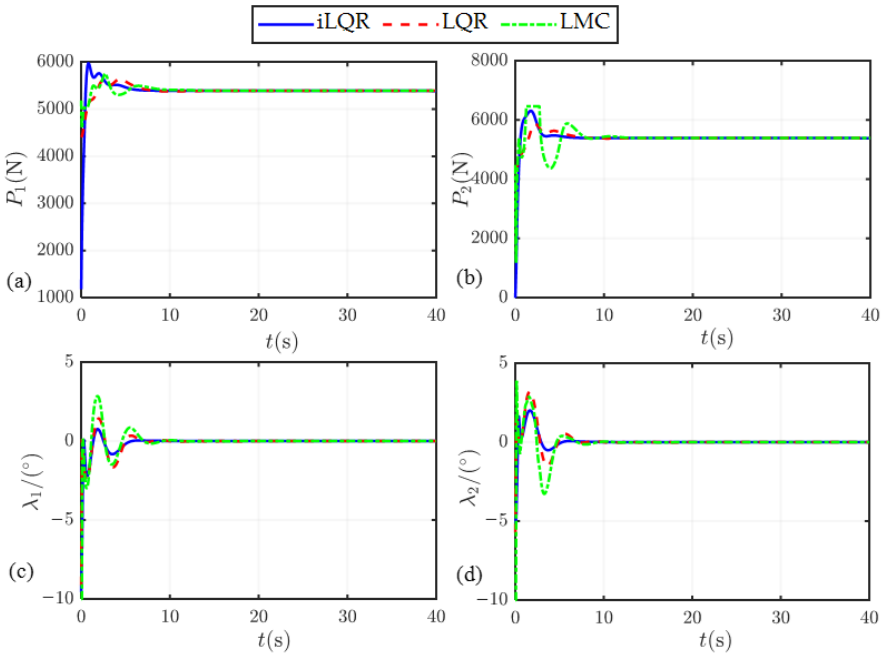


Figure 10. Variation curves of the control variables of the DUH-SLS. (**a**) Variation curves of UAH1's rotor thrust; (**b**) variation curves of UAH2's rotor thrust; (**c**) variation curves of UAH1's rotor thrust direction angle; (**d**) variation curves of UAH2's rotor thrust direction angle.

Based on Figure 10 and Table 5, it can be observed that the variation amplitude of P_1 is smaller than that of P_2, whereas the variation amplitude of the thrust direction angle exhibits the opposite trend. Examining the variation curves of UAH2's control variables, it is found that under the iLQR optimal controller, the peak value of P_2 is slightly higher than that under the LQR controller but lower than that under the LMC controller. Moreover, the peak value of λ_2 is smaller and its variation is smoother compared to the other two controllers.

According to Figures 8–10 and Table 5, the iLQR optimal controller demonstrates its effectiveness. It successfully reduces the peak values and oscillations of the control variables. Additionally, it achieves a higher level of control accuracy. This characteristic is of great significance in practical dual-UAH cooperative transportation tasks: lower peaks and oscillations of control variables can reduce actuator energy consumption, alleviate mechanical loads, extend equipment lifespan, and enhance the smoothness and safety of load transportation. These results demonstrate the superiority and engineering potential of the iLQR optimal controller in complex slung load missions.

To evaluate the robustness of the iLQR controller, simulations were conducted under two working conditions: with suspended loads of 240 kg (−20% of the nominal value) and 380 kg (+26.67% of the nominal value). Since the focus is on position tracking and swing suppression performance, only the time response curves of the suspended load position

and swing angle are presented in the following sections (the system pitch angle variations are similar and are omitted for brevity). The simulation results are shown in Figure 11.

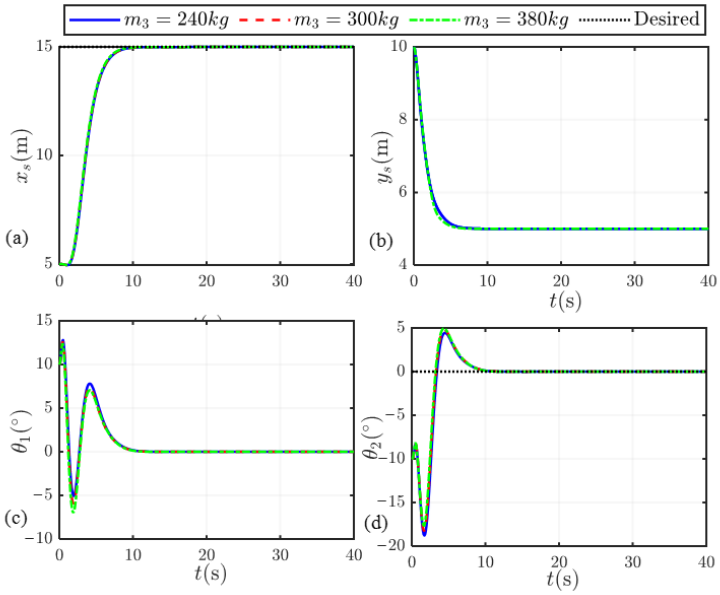


Figure 11. State response curves (position and swing angles) of the DUH-SLS with different suspended load masses. (**a**) Variation curves of the X-coordinate of the suspended load's centroid; (**b**) variation curves of the Y-coordinate of the suspended load's centroid; (**c**) variation curves of the swing angle of cable 1; (**d**) variation curves of the swing angle of cable 2.

According to the simulation results in Figure 11, the iLQR controller maintains high position tracking accuracy and effective swing suppression even under variations in the suspended load mass. The state response curves are nearly identical, demonstrating their good parameter adaptation capability and robustness.

To further evaluate the robustness boundaries of the iLQR controller and determine its stability limits, robustness simulation analyses under wide-range payload variations are conducted in this section. Based on the rotor thrust limits of a single UAH (as shown in Table 5), the theoretical maximum suspended load mass is calculated as 526.5 kg. To comprehensively test the controller performance, the nominal suspended load mass is set to 300 kg, and the simulation covers a range from 200 kg (−33.3% of the nominal value) to 540 kg (+80% of the nominal value, approximately 102.6% of the theoretical maximum load mass). This range encompasses both normal operational fluctuations (−33%) and extreme conditions approaching the physical limits (+80%), ensuring comprehensive and challenging testing scenarios.

Based on the Monte Carlo method, the suspended load mass is increased from 200 kg to 540 kg with a step size of 10 kg, resulting in a total of 35 mass conditions. For each condition, 20 independent simulations are conducted with random initial disturbances to simulate real-world uncertainties. For all tested conditions, the mean, standard deviation, and 95% confidence intervals of tracking error and maximum swing angle are calculated.

To quantitatively evaluate the robustness and control performance of the iLQR controller under varying payload masses, statistical analysis based on the Monte Carlo method is conducted in this section. For each payload condition, 20 independent simulation runs are performed with random initial disturbances. For each simulation run, the following evaluation metrics are defined:

(1) Position Tracking Error

$x_{s,n+1}$ and $y_{s,n+1}$ represent the terminal position state values of the simulation. For the i-th simulation run, the terminal position tracking error is defined below.

For the i-th simulation run, the instantaneous position tracking error is defined as

$$e_{p,i} = \sqrt{(x_{s,n+1} - x_s^c)^2 + (y_{s,n+1} - y_s^c)^2} \tag{35}$$

(2) Terminal Swing Suppression Error

$\theta_{1,n+1}$ and $\theta_{2,n+1}$ represent the terminal swing angle state values of the simulation, with desired angles of 0°. For the i-th simulation run, the instantaneous errors of the two angles at the final time instant are

$$e_{\theta_1,i} = |\theta_{1,n+1}| \tag{36}$$

(**Note:** Due to the symmetric configuration and consistent swing trends observed between the two helicopters in the DUH-SLS, only θ_1 is presented as a representative metric for swing suppression performance. The analysis for θ_2 yields similar results and is omitted for brevity.)

(3) Statistical Metrics Calculation

For each payload condition, based on the $e_{p,i}$ and $e_{\theta_1,i}$ values $(i = 1, 2, \ldots, N; N = 20)$ from 20 independent simulation runs, the following statistical metrics are computed.

Mean μ represents the average level of control performance, which is defined as

$$\mu = \frac{1}{N}\sum_{i=1}^{N} e_i \tag{37}$$

Standard deviation σ (defined as Equation (38)) quantifies the dispersion among multiple simulation runs, reflecting the stability of control performance.

$$\sigma = \sqrt{\frac{1}{N}\sum_{i=1}^{N} (e_i - \mu)^2} \tag{38}$$

The 95% confidence interval $\mu \pm 1.96 \times \frac{\sigma}{\sqrt{N}}$ indicates the range within which the true mean lies with 95% confidence.

The simulation results are shown in Figure 12 and Table 6. Table 6 summarizes the simulation results for selected typical payload masses (200–510 kg), derived from 20 Monte Carlo runs per condition.

Table 6. Statistical results of iLQR controller performance under selected payload conditions (based on 20 Monte Carlo simulations).

Suspended Load (kg)	Position Error (m) $\mu \pm \sigma$	95% Confidence Interval (m)	θ_1 Error (Deg) $\mu \pm \sigma$	95% Confidence Interval (Deg)	Status
200	0.031 ± 0.005	[0.029, 0.033]	$(5.20 \pm 0.80) \times 10^{-4}$	$[4.85, 5.55] \times 10^{-4}$	Stable
300	0.042 ± 0.007	[0.039, 0.045]	$(6.00 \pm 1.00) \times 10^{-4}$	$[5.56, 6.44] \times 10^{-4}$	Stable
400	0.055 ± 0.009	[0.051, 0.059]	$(7.20 \pm 1.30) \times 10^{-4}$	$[6.63, 7.77] \times 10^{-4}$	Stable
500	0.064 ± 0.012	[0.059, 0.069]	$(8.60 \pm 1.80) \times 10^{-4}$	$[7.81, 9.39] \times 10^{-4}$	Stable
510	0.068 ± 0.018	[0.060, 0.076]	$(1.00 \pm 0.25) \times 10^{-3}$	$[8.90, 11.1] \times 10^{-4}$	Marginally Stable

Figure 12 and Table 6 show key simulation metrics across different suspended load masses, including the load's final position tracking error, swing angle tracking error, maximum rotor thrust for UAH1 and UAH2, and iLQR controller stability. Integrating these simulation results, it is evident that the iLQR controller demonstrates excellent control performance and stability when the suspended load's mass is below approximately 500 kg. It is capable of effectively maintaining system stability even in the presence of parameter

perturbations. However, when the suspended load mass exceeds 510 kg, the control performance and stability of the iLQR controller significantly deteriorate, despite this mass still being below the maximum load the system can bear. Once the maximum mass of the suspended load is exceeded, the iLQR controller can no longer guarantee stability. Specifically, the iLQR controller can achieve effective control performance and ensure system stability and reliability as long as the suspended payload mass remains below 94.97% of the maximum theoretical suspended load mass.

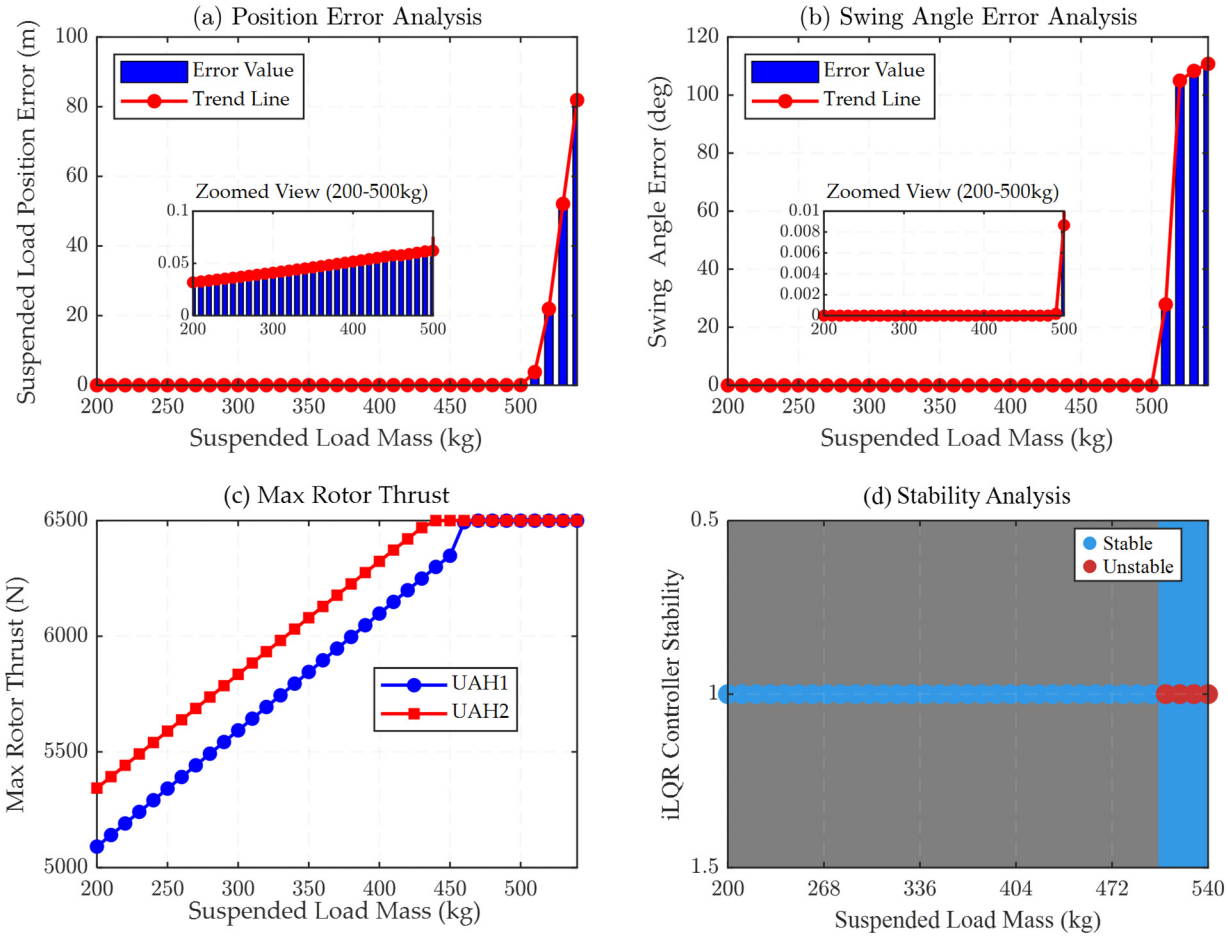


Figure 12. Variation in iLQR controller performance with increasing suspended load mass. (**a**) Maximum tracking error of the suspended load's position; (**b**) maximum tracking error of the swing angle; (**c**) maximum rotor thrusts of UAH1 and UAH2; (**d**) stability of the iLQR Controller.

These demonstrate that the iLQR optimal controller exhibits great robustness when confronted with internal parameter uncertainties, effectively ensuring the control performance and reliability of the DUH-SLS in practical applications.

In actual flight operations, wind disturbance constitutes an important external factor affecting system stability and control precision. Various wind fields in complex atmospheric environments directly act on the UAH and its suspended load, inducing significant positional deviations and load swing, which may severely compromise flight safety. Therefore, this study validates the effectiveness and robustness of the iLQR controller under a horizontal wind disturbance from the right side (the DUH-SLS's dynamics modeling process incorporating the wind disturbance is detailed in Appendix A). Simulations are conducted for two typical scenarios: constant wind speed and time-varying wind speed, respectively.

The wind speed from the right side is set as V_{air}. Two constant wind speeds are specified as follows:

$$\left\{ V_{\text{air}} = 5\ \text{m} \cdot \text{s}^{-1}, V_{\text{air}} = 10\ \text{m} \cdot \text{s}^{-1} \right. \tag{39}$$

Three typical time-varying wind speed models are adopted for simulation: a sinusoidally varying wind speed, a step wind speed, and a gust wind speed. Their mathematical models are described by Equation (40). (In the following equation, the wind speed V_{air} has units of $\text{m} \cdot \text{s}^{-1}$, and time t has units of second.)

$$\begin{cases} V_{\text{air}}(t) = 5 + 3\sin(0.5t) \\ V_{\text{air}}(t) = \begin{cases} 5, \ 0 \le t < 25 \\ 10, \ 25 \le t \le 50 \end{cases} \\ V_{\text{air}}(t) = \begin{cases} 3 + 8 \cdot \exp(20 - t) \cdot \exp(10 - 0.5t)\ , \ 20 \le t \le 25 \\ 3 \qquad\qquad\qquad\qquad\qquad\qquad\qquad\quad , \text{ else} \end{cases} \end{cases} \tag{40}$$

The simulation input parameters are the same as those mentioned earlier in this section and the numerical simulation results are shown in Figures 13 and 14.

Based on the results shown in Figures 13 and 14, it can be concluded that the iLQR optimal controller enables the system to track from the initial position to the hover position under both constant and time-varying wind fields while effectively suppressing the swing of the suspended load. Both constant and time-varying wind fields lead to certain steady-state errors in the longitudinal displacement x_s of the suspended load and the swing angles θ_1, θ_2, with the steady-state error increasing as the wind speed rises. Nevertheless, all errors remain within 5%, indicating that the iLQR optimal controller exhibits excellent control performance and strong robustness in the presence of external wind disturbances.

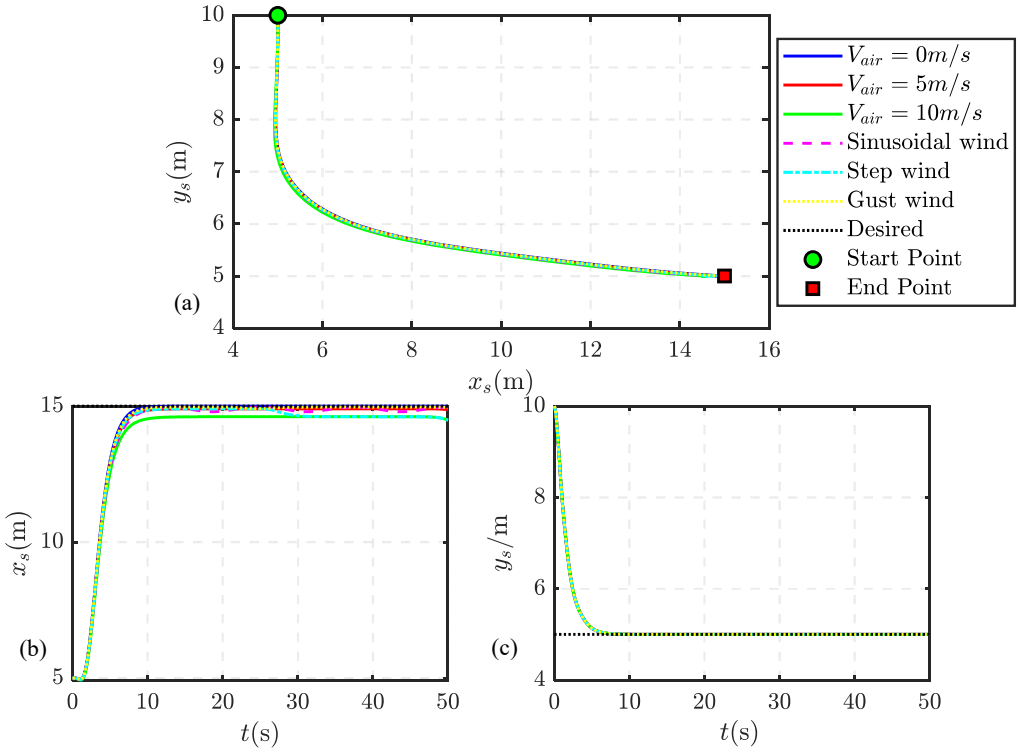


Figure 13. Trajectory curves of the suspended load's centroid position and position state response curves. (**a**) Load's trajectory curves; (**b**) variation curves of the X-coordinate of the load's centroid; (**c**) variation curves of the Y-coordinate of the load's centroid.

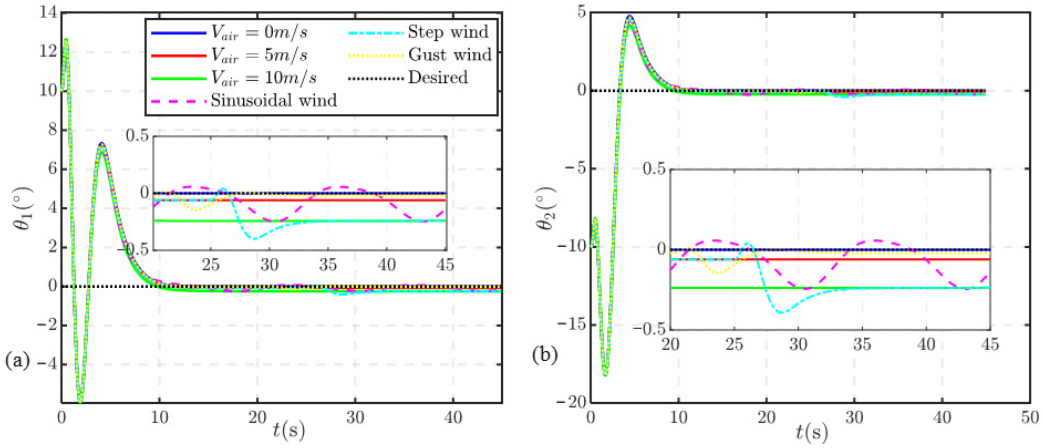


Figure 14. Swing angles 1,2 response curves of the suspended load. (**a**) variation curves of the swing angle of cable 1; (**b**) variation curves of the swing angle of cable 2.

4.2. Task Scenario 2: Trajectory Tracking

The trajectory to be tracked by the DUH-SLS is an elliptical reference trajectory defined with respect to the centroid of the suspended load. Its time-parametric equations are given as follows:

$$\begin{cases} x_s^c = 12\sin(\frac{\pi}{25}t), \ y_s^c = 5 + 5\cos(\frac{\pi}{25}t) \end{cases} \tag{41}$$

Two trajectory tracking simulation working conditions are considered below.

Condition 1: During the trajectory tracking process, both the suspension swing angles of the DUH-SLS will converge to the command values, i.e.,

$$\{\theta_1^c = 0, \ \theta_2^c = 0 \tag{42}$$

Condition 2: During the trajectory tracking process, the DUH-SLS will maintain the swing angles at the command values, i.e.,

$$\begin{cases} \theta_1^c = 10^\circ, \ \theta_2^c = -10^\circ \end{cases} \tag{43}$$

Condition 2 represents a typical scenario in dual-UAH slung load transportation. In this condition, by appropriately controlling the swing angles to maintain a fixed value, a safe distance between the two UAHs can be effectively ensured, thereby guaranteeing the reliability and safety of task execution. This scenario also imposes higher requirements on the stability and robustness of the controller, providing a comprehensive test of its adaptability and control performance in complex dynamic environments.

The simulation input parameters for this scenario are listed in Table 7, while other simulation input parameters are provided in Tables 3 and 4.

Table 7. Trajectory Tracking: Simulation input parameters.

Parameter/Unit	Value	Parameter/Unit	Value
$(x_{s0}, y_{s0})/\mathrm{m}$	$(12, 10)$	$\eta_{10}/^\circ$	0
$\theta_{10}/^\circ$	0	$\eta_{20}/^\circ$	0
$\theta_{20}/^\circ$	0	$\varepsilon_0/^\circ$	0

The numerical simulation results under the two working conditions are shown in Figures 15–18.

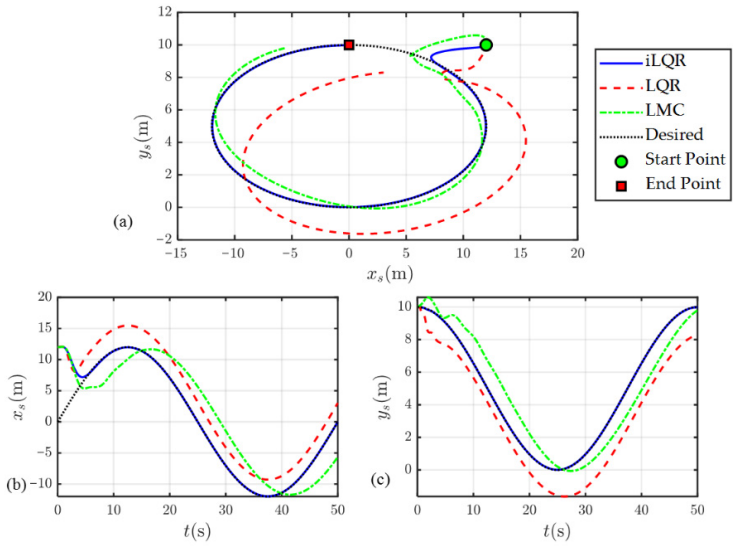


Figure 15. Trajectory tracking results of the DUH-SLS under Condition 1: Trajectory tracking curves of the suspended load. (**a**) Load centroid trajectory variation curves; (**b**) variation curves of the X-coordinate of the load's centroid; (**c**) variation curves of the Y-coordinate of the load's centroid.

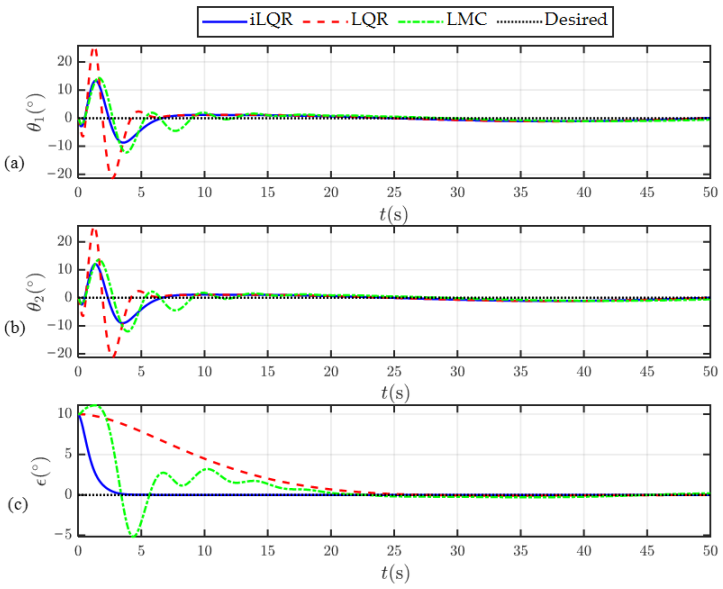


Figure 16. Trajectory tracking results of the DUH-SLS under Condition 1: Variation curves of swing angles and the pitch angle of the suspended load. (**a**) Variation curves of UAH1's pitch angle; (**b**) variation curves of UAH2's pitch angle; (**c**) variation curves of the load's pitch angle.

To quantitatively evaluate the trajectory tracking performance of the DHU-SLS, a tracking error evaluation metric is defined as shown in Equation (44). Here, $e(t)$ represents the instantaneous trajectory tracking error; e_{ss} denotes the steady-state average error, which is used to measure the steady-state tracking accuracy of the controller; t_s indicates the time when the system enters the steady state; and σ_{ss}^2 represents the variance of the tracking error, reflecting the fluctuation level of the tracking error.

$$\begin{cases} e(t_i) = \sqrt{[x_s(t_i) - x_s^c(t_i)]^2 + [y_s(t_i) - y_s^c(t_i)]^2} \\ e_{ss} = \dfrac{1}{N}\sum_{i=1}^{N} e(t_i) \\ \sigma_{ss}^2 = \dfrac{1}{N}\sum_{i=1}^{N} [e(t_i) - e_{ss}]^2 \end{cases}, \; t_i \in [0, 50] \tag{44}$$

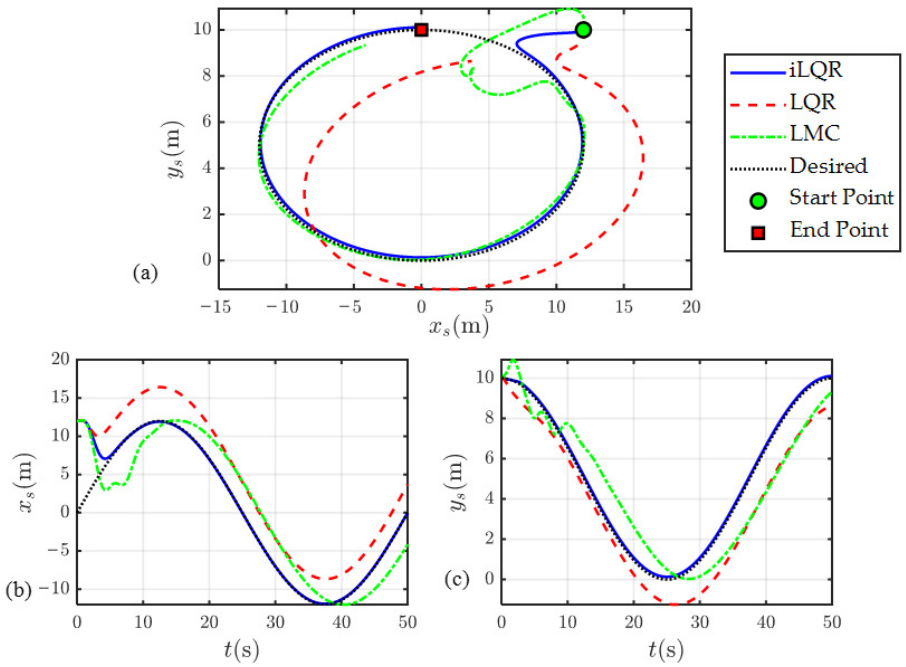


Figure 17. Trajectory tracking results of the DUH-SLS under Condition 2: Trajectory tracking curves of the suspended load. (**a**) Load centroid trajectory variation curves; (**b**) variation curves of the X-coordinate of the load's centroid; (**c**) variation curves of the Y-coordinate of the load's centroid.

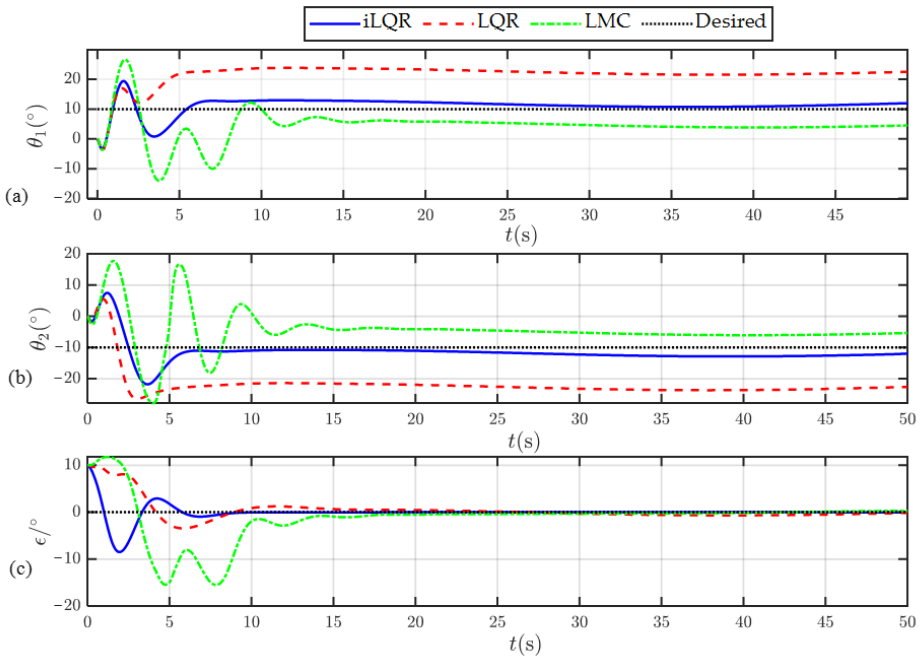


Figure 18. Trajectory tracking results of the DUH-SLS under Condition 2: Variation curves of swing angles and the pitch angle of the suspended load. (**a**) Variation curves of UAH1's pitch angle; (**b**) variation curves of UAH2's pitch angle; (**c**) variation curves of the load's pitch angle.

The trajectory tracking error curves of the DUH-SLS under the two different conditions are shown in Figure 19.

Figures 15 and 17 present the position trajectory tracking curves under the two different working conditions. It can be observed that the iLQR optimal controller enables rapid convergence to and precise tracking of the predefined reference trajectory. In contrast, the responses of the LQR and LMC controllers are relatively delayed and exhibit lower tracking accuracy. As shown in Figure 19a, under Condition 2, the tracking accuracy of the

LQR controller decreases significantly. In contrast, the tracking accuracy of the iLQR and LMC controllers only declines slightly, with the iLQR optimal controller still maintaining high precision. Comprehensive analysis of Figures 15, 17 and 19a indicates that the iLQR optimal controller demonstrates superior performance under both working conditions, achieving faster convergence speed and higher tracking accuracy.

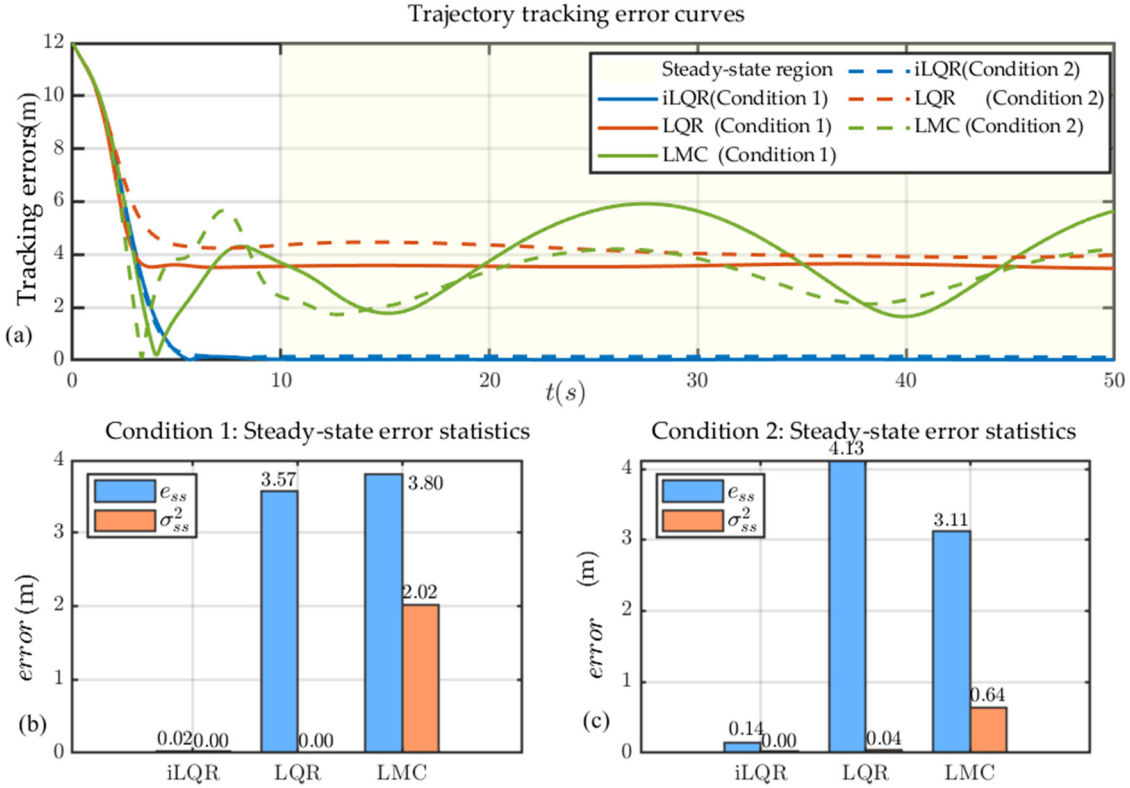


Figure 19. Trajectory tracking error curves. (**a**) Trajectory tracking error curves. (**b**) Condition 1: Steady-state error statistics; (**c**) Condition 2: Steady-state error statistics.

Quantitative analysis based on Figure 19 shows that the steady-state average errors of iLQR under both operating conditions are 0.02 m and 0.14 m, significantly lower than those of LQR (3.57 m and 4.13 m) and LMC (3.86 m and 3.11 m). In terms of error variance, iLQR remains near zero in both cases, indicating stable tracking with minimal fluctuation. While LQR exhibits small variance, its absolute error is large. LMC shows the highest variance (2.02 m in condition 1 and 0.64 m in condition 2), with noticeable error magnitude and fluctuation. Overall, iLQR demonstrates clearly superior tracking accuracy and stability, validating its effectiveness and advantage in handling nonlinear trajectory tracking for the DUH-SLS.

Figures 16 and 18 show the variation curves of the swing angles and the pitch angle of the suspended load under the two working conditions. Under Condition 1, the swing angles and the pitch angle of the suspended load converge to their command values with oscillations under all three controllers. However, the iLQR optimal controller significantly reduces the oscillation amplitude of the swing angles and achieves faster convergence, while also providing better dynamic performance for the pitch angle of the suspended load. Under Condition 2, with the application of iLQR, LQR, and LMC, θ_1 converges in oscillation within 9.5–10.5°, 11.8–12.8°, and 5.6–6.4°. Only the iLQR optimal controller can damp the swing angle θ_1 to the command values, and its dynamic characteristics during the convergence process are superior to the other two controllers. The change trends of θ_2 are similar and thus omitted for brevity.

Overall, as shown in Figures 16, 18 and 19, the dynamic performance of the system's state response curves under Condition 2 deteriorates significantly, indicating a higher level of control difficulty. Nevertheless, the iLQR optimal controller still achieves relatively optimal control performance. The iLQR controller exhibits significant advantages in improving trajectory-tracking accuracy and suppressing the swing of the suspended load. In particular, in complex scenarios, this controller is capable of rapidly tracking the reference trajectory and maintaining the desired swing angles with high precision.

5. Conclusions

5.1. Summary of This Paper

In this paper, a set of independent and complete generalized coordinates of DUH-SLS is skillfully selected, and a seven-degrees-of-freedom (DOFs) dynamics model for the DUH-SLS is established based on Lagrange analytical mechanics, without considering ideal internal constraint forces. This approach significantly enhances the modeling efficiency of multi-body coupled systems and provides a solid foundation for subsequent controller design. To address safety issues caused by suspended load swing, the iLQR method is introduced to design an integrated nonlinear optimal controller for trajectory tracking and swing suppression of the DUH-SLS. To evaluate the performance advantages of the iLQR optimal controller, the traditional LQR optimal controller and the LMC nonlinear controller are also implemented for comparison, and extensive numerical simulations are conducted under various scenarios and working conditions. The main conclusions are as follows:

(1) A virtual prototype of the DUH-SLS is constructed in ADAMS software, and numerical simulations are conducted for both the virtual prototype and the dynamics model proposed in this paper under identical working conditions. The simulation results demonstrate the correctness of the dynamics model established in this study for the DUH-SLS.

(2) In complex scenarios, such as hovering control and trajectory tracking tasks, the iLQR optimal controller demonstrates superior control performance and accuracy compared to the traditional LQR optimal controller and the LMC nonlinear controller. The iLQR controller effectively suppresses load swing and achieves rapid, high-precision tracking of reference trajectories, thereby meeting the stringent safety and reliability requirements of DUH-SLS in challenging tasks. This advantage stems from the iLQR method's ability to effectively handle the strong nonlinearities and coupling characteristics of the system through iterative optimization in function space.

(3) The iLQR optimal controller exhibits good robustness in the presence of internal parameter uncertainties and external complex wind disturbances, demonstrating its engineering application potential in real-world complex environments.

In summary, this work systematically investigates the dynamics characteristics and control strategies of DUH-SLS through a combination of theoretical modeling and simulation validation. The design and application of the iLQR optimal controller not only enrich the theoretical framework for controlling underactuated nonlinear systems and provide new insights for handling strongly coupled, highly nonlinear multi-body systems, but also provide an efficient and reliable solution for complex slung load missions.

5.2. Limitations and Future Work

The research outcomes of this study can be extended to various practical application scenarios, including but not limited to collaborative transportation of heavy tower materials in mountainous terrain for power infrastructure construction, precision delivery of supplies in complex environments for emergency rescue operations, collaborative handling of heavy equipment in ports or warehouses, and aerial deployment of large-scale fire retardants in forest fire suppression missions. These scenarios commonly face challenges such as

heavy payloads, complex terrain, and high-precision control requirements—precisely the domains where the proposed approach demonstrates its advantages.

However, this study has the following limitations: the current dynamics model is confined to the two-dimensional plane, and physical experimental validation has not been conducted due to laboratory constraints. Real-world issues such as sensor noise, communication delays, aerodynamic interference, and actuator saturation have not been fully considered. Future work will focus on establishing a sixteen-degree-of-freedom three-dimensional dynamics model for the DUH-SLS and conducting physical experiments to address these engineering challenges, thereby facilitating the transition of the proposed method toward practical applications.

Author Contributions: Conceptualization, Y.H.; Methodology, Y.H. and R.L.; Software, R.L.; Investigation, Y.Z.; Resources, Y.Z.; Writing—original draft, R.L.; Writing—review & editing, Y.H.; Supervision, Y.H. Project administration, Y.H. All authors have read and agreed to the published version of the manuscript.

Funding: This research received no external funding.

Data Availability Statement: The original contributions presented in the study are included in the article, further inquiries can be directed to the corresponding author.

Conflicts of Interest: The authors declare no conflicts of interest.

Appendix A

The schematic diagram of the DUH-SLS subjected to a directional wind from the right side is shown below.

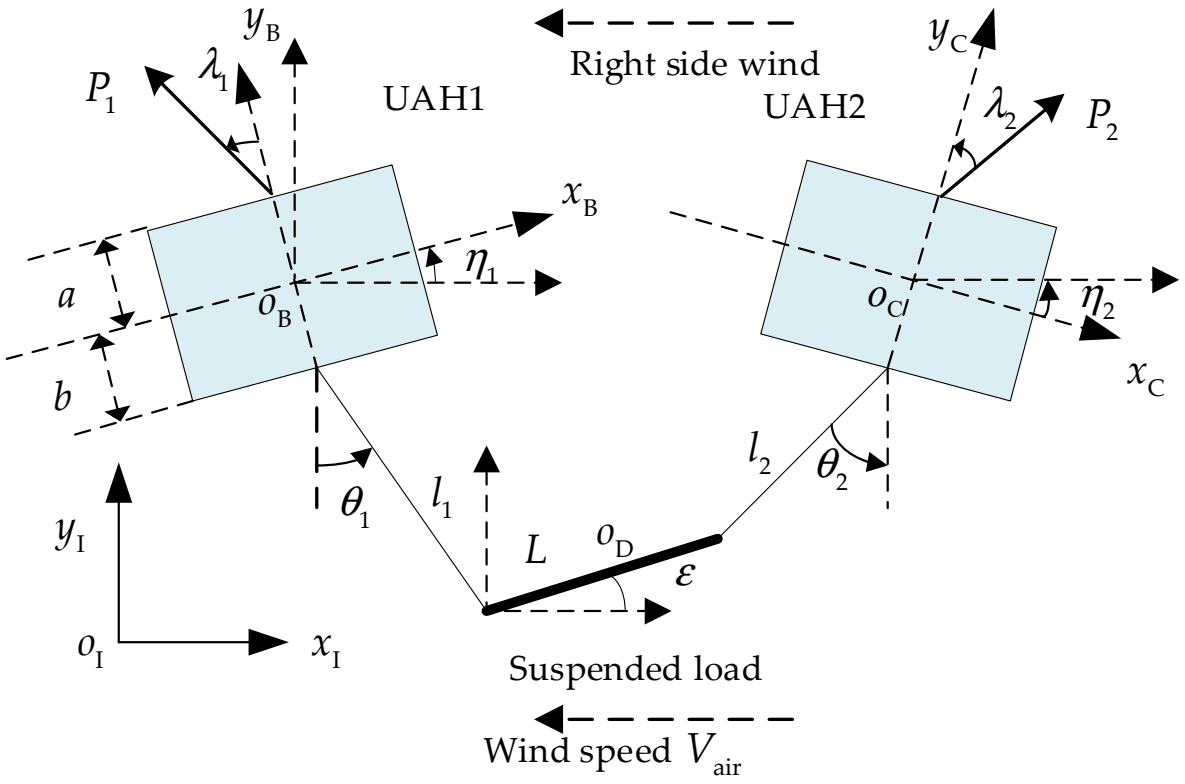


Figure A1. Schematic diagram of the longitudinal plane simplified model of DUH-SLS under wind disturbance.

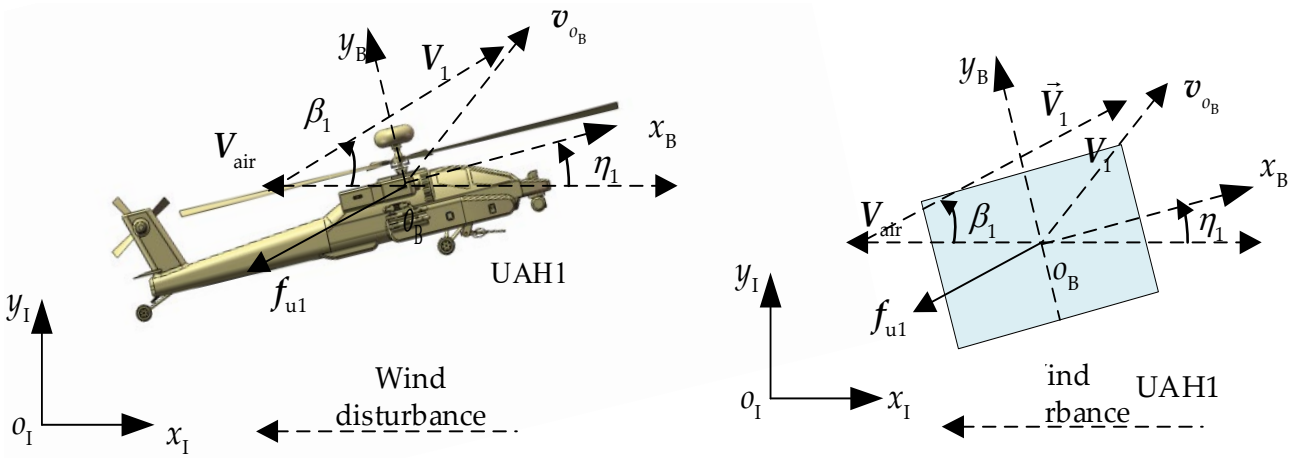


Figure A2. Schematic diagram of the relative wind speed and aerodynamic drag direction of UAH1.

$$
\begin{cases}
(m_1+m_2+m_3)\ddot{x}_s - m_1 l_1\cos\theta_1\ddot{\theta}_1 - m_2 l_2\cos\theta_2\ddot{\theta}_2 - m_1 b\cos\eta_1\ddot{\eta}_1 - m_2 b\cos\eta_2\ddot{\eta}_2 + \frac{L}{2}\sin\varepsilon(m_1-m_2)\ddot{\varepsilon} \\
+m_1(\frac{L}{2}\dot{\varepsilon}^2\cos\varepsilon + l_1\dot{\theta}_1^2\sin\theta_1 + b\dot{\eta}_1^2\sin\eta_1) + m_2(-\frac{L}{2}\dot{\varepsilon}^2\cos\varepsilon + l_2\dot{\theta}_2^2\sin\theta_2 + b\dot{\eta}_2^2\sin\eta_2) \\
+P_1\sin(\eta_1+\lambda_1) + P_2\sin(\eta_2+\lambda_2) - f_{u1x} - f_{u2x} - f_{sx} = 0 \\
\\
(m_1+m_2+m_3)\ddot{y}_s - m_1 l_1\sin\theta_1\ddot{\theta}_1 - m_2 l_2\sin\theta_2\ddot{\theta}_2 - m_1 b\sin\eta_1\ddot{\eta}_1 - m_2 b\sin\eta_2\ddot{\eta}_2 + \frac{L}{2}\cos\varepsilon(m_2-m_1)\ddot{\varepsilon} \\
-m_1(-\frac{L}{2}\dot{\varepsilon}^2\sin\varepsilon + l_1\dot{\theta}_1^2\cos\theta_1 + b\dot{\eta}_1^2\cos\eta_1) + m_2(-\frac{L}{2}\dot{\varepsilon}^2\sin\varepsilon - l_2\dot{\theta}_2^2\sin\theta_2 - b\dot{\eta}_2^2\sin\eta_2) \\
+(m_1+m_2+m_3)g - P_1\cos(\eta_1+\lambda_1) - P_2\cos(\eta_2+\lambda_2) - f_{u1y} - f_{u2y} - f_{sy} = 0 \\
\\
-m_1 l_1\cos\theta_1\ddot{x}_s - m_1 l_1\sin\theta_1\ddot{y}_s + m_1 l_1^2\ddot{\theta}_1 + m_1 b l_1\cos(\eta_1-\theta_1)\ddot{\eta}_1 + \frac{L}{2}m_1 l_1\sin(\theta_1-\varepsilon)\ddot{\varepsilon} - \frac{L}{2}m_1 l_1\dot{\varepsilon}^2\cos(\theta_1-\varepsilon) \\
-m_1 b l_1\sin(\eta_1-\theta_1)\dot{\eta}_1^2 - m_1 g l_1\sin\theta_1 - P_1 l_1\sin(\eta_1+\lambda_1-\theta_1) + l_1(f_{u1x}\cos\theta_1 + f_{u1y}\sin\theta_1) = 0 \\
\\
-m_2 l_2\cos\theta_2\ddot{x}_s - m_2 l_2\sin\theta_2\ddot{y}_s + m_2 l_2^2\ddot{\theta}_2 + m_2 b l_2\cos(\eta_2-\theta_2)\ddot{\eta}_2 - \frac{L}{2}m_2 l_2\sin(\theta_2-\varepsilon)\ddot{\varepsilon} + \frac{L}{2}m_2 l_2\dot{\varepsilon}^2\cos(\theta_2-\varepsilon) \\
-m_2 b l_2\sin(\eta_2-\theta_2)\dot{\eta}_2^2 - m_2 g l_2\sin\theta_2 - P_2 l_2\sin(\eta_2+\lambda_2-\theta_2) + l_2(f_{u2x}\cos\theta_2 + f_{u2y}\sin\theta_2) = 0 \\
\\
-m_1 b\cos\eta_1\ddot{x}_s - m_1 b\sin\eta_1\ddot{y}_s + m_1 b l_1\cos(\eta_1-\theta_1)\ddot{\theta}_1 + (I_1+m_1 b^2)\ddot{\eta}_1 + \frac{L}{2}m_1 b\sin(\eta_1-\varepsilon)\ddot{\varepsilon} - \frac{L}{2}m_1 b\dot{\varepsilon}^2\cos(\eta_1-\varepsilon) \\
+m_1 b l_1\sin(\eta_1-\theta_1)\dot{\theta}_1^2 - m_1 g b\sin\eta_1 - (a+b)P_1\sin\lambda_1 + b(f_{u1x}\cos\eta_1 + f_{u1y}\sin\eta_1) = 0 \\
\\
-m_2 b\cos\eta_2\ddot{x}_s - m_2 b\sin\eta_2\ddot{y}_s + m_2 b l_2\cos(\eta_2-\theta_2)\ddot{\theta}_2 + (I_2+m_2 b^2)\ddot{\eta}_2 - \frac{L}{2}m_2 b\sin(\eta_2-\varepsilon)\ddot{\varepsilon} + \frac{L}{2}m_2 b\cos(\eta_2-\varepsilon)\dot{\varepsilon}^2 \\
+m_2 b l_2\sin(\eta_2-\theta_2)\dot{\theta}_2^2 - m_2 g b\sin\eta_2 - (a+b)P_2\sin\lambda_2 + b(f_{u2x}\cos\eta_2 + f_{u2y}\sin\eta_2) = 0 \\
\\
\frac{L}{2}(m_1-m_2)\sin\varepsilon\ddot{x}_s + \frac{L}{2}(m_2-m_1)\cos\varepsilon\ddot{y}_s + \frac{L}{2}m_1 l_1\sin(\theta_1-\varepsilon)\ddot{\theta}_1 - \frac{L}{2}m_2 l_2\sin(\theta_2-\varepsilon)\ddot{\theta}_2 + \frac{L}{2}m_1 b\sin(\eta_1-\varepsilon)\ddot{\eta}_1 \\
-\frac{L}{2}m_2 b\sin(\eta_2-\varepsilon)\ddot{\eta}_2 + (\frac{L^2}{4}m_1 + \frac{L^2}{4}m_2 + I_3)\ddot{\varepsilon} + \frac{L}{2}m_1 l_1\cos(\theta_1-\varepsilon)\dot{\theta}_1^2 + \frac{L}{2}m_1 b\cos(\eta_1-\varepsilon)\dot{\eta}_1^2 \\
-\frac{L}{2}m_2 l_2\cos(\theta_2-\varepsilon)\dot{\theta}_2^2 - \frac{L}{2}m_2 b\cos(\eta_2-\varepsilon)\dot{\eta}_2^2 - \frac{L}{2}m_1 g\cos\varepsilon + \frac{L}{2}m_2 g\cos\varepsilon + \frac{L}{2}P_1\cos(\eta_1+\lambda_1-\varepsilon) \\
-\frac{L}{2}P_2\cos(\eta_2+\lambda_2-\varepsilon) - \frac{L}{2}[(f_{u1x}-f_{u2x})\sin\varepsilon + (f_{u2y}-f_{u1y})\cos\varepsilon] = 0
\end{cases}
\tag{A1}
$$

The relationship between the UAH's motion direction and airflow direction is illustrated in Figure A2. Through theoretical analysis and mathematical derivation, the system dynamics model incorporating wind disturbance can be obtained as shown in Equation (A1).

The projection column matrices of the disturbance drags generated by the wind on the UAH1 and UAH2 in the I-frame are

$$
\begin{cases}
\boldsymbol{f}_{u1} = \boldsymbol{I}(-f_1\cos\beta_1, -f_1\sin\beta_1)_I^T \triangleq \boldsymbol{I}(f_{1ux}, f_{1uy})_I^T \\
f_1 = \frac{1}{2}C_d\rho S_1\|\boldsymbol{V}_1\|^2 \\
\boldsymbol{f}_{u2} = \boldsymbol{I}(-f_2\cos\beta_2, -f_2\sin\beta_2)_I^T \triangleq \boldsymbol{I}(f_{2ux}, f_{2uy})_I^T \\
f_2 = \frac{1}{2}C_d\rho S_2\|\boldsymbol{V}_2\|^2
\end{cases}
\tag{A2}
$$

where

$$\begin{cases} \boldsymbol{V}_1 = \boldsymbol{v}_{o_\mathrm{B}} - \boldsymbol{V}_{air} = \boldsymbol{I}(v_{o_\mathrm{B}x} + V_{air}, v_{o_\mathrm{B}y})_\mathrm{I}^\mathrm{T} \\ \boldsymbol{v}_{o_\mathrm{B}} = \boldsymbol{I}\begin{pmatrix} \dot{x}_\mathrm{s} + \frac{L}{2}\sin\varepsilon\dot{\varepsilon} - l_1\cos\theta_1\dot{\theta}_1 - b\cos\eta_1\dot{\eta}_1 \\ \dot{y}_\mathrm{s} - \frac{L}{2}\cos\varepsilon\dot{\varepsilon} - l_1\sin\theta_1\dot{\theta}_1 - b\sin\eta_1\dot{\eta}_1 \end{pmatrix}_\mathrm{I} \triangleq \boldsymbol{I}\begin{pmatrix} v_{o_\mathrm{B}x} \\ v_{o_\mathrm{B}y} \end{pmatrix}_\mathrm{I} \\ \beta_1 = \mathrm{acrtan}(\frac{v_{o_\mathrm{B}y}}{v_{o_\mathrm{B}x}+V_\mathrm{air}}) \end{cases} \quad (A3)$$
$$\begin{cases} \boldsymbol{V}_2 = \boldsymbol{v}_{o_\mathrm{C}} - \boldsymbol{V}_\mathrm{air} = \boldsymbol{I}(v_{2x} + V_\mathrm{air}, v_{2y})_\mathrm{A}^\mathrm{T} \\ \boldsymbol{v}_{o_\mathrm{C}} = \boldsymbol{I}\begin{pmatrix} \dot{x}_\mathrm{s} - \frac{L}{2}\sin\varepsilon\dot{\varepsilon} - l_2\cos\theta_2\dot{\theta}_2 - b\cos\eta_2\dot{\eta}_2 \\ \dot{y}_\mathrm{s} + \frac{L}{2}\cos\varepsilon\dot{\varepsilon} - l_2\sin\theta_2\dot{\theta}_2 - b\sin\eta_2\dot{\eta}_2 \end{pmatrix}_\mathrm{I} \triangleq \boldsymbol{I}\begin{pmatrix} v_{o_\mathrm{C}x} \\ v_{o_\mathrm{C}y} \end{pmatrix}_\mathrm{I} \\ \beta_2 = \mathrm{acrtan}(\frac{v_{o_\mathrm{C}y}}{v_{o_\mathrm{C}x}+V_\mathrm{air}}) \end{cases}$$

The projection column matrix of the disturbance drags generated by the wind on the suspended load in the I-frame is

$$\begin{cases} f_\mathrm{s} = \boldsymbol{I}(-f_3\cos\beta_3, -f_3\sin\beta_3)_\mathrm{I}^\mathrm{T} \triangleq \boldsymbol{I}(f_{\mathrm{s}x}, f_{\mathrm{s}y})_\mathrm{I}^\mathrm{T} \\ f_3 = \frac{1}{2}C_\mathrm{d}\rho S_3\|\boldsymbol{V}_3\|^2 \end{cases} \quad (A4)$$

where

$$\begin{cases} \boldsymbol{V}_3 = \boldsymbol{v}_{o_\mathrm{D}} - \boldsymbol{V}_\mathrm{air} = \boldsymbol{I}(v_{o_\mathrm{D}x} + V_\mathrm{air}, v_{o_\mathrm{D}y})_\mathrm{I}^\mathrm{T} \\ \boldsymbol{v}_{o_\mathrm{D}} \triangleq \boldsymbol{I}(v_{o_\mathrm{D}x}, v_{o_\mathrm{D}y})_\mathrm{I}^\mathrm{T} = (\dot{x}_\mathrm{s}, \dot{y}_\mathrm{s})_\mathrm{I}^\mathrm{T} \\ \beta_3 = \mathrm{acrtan}(\frac{\dot{y}_\mathrm{s}}{\dot{x}_\mathrm{s}+V_\mathrm{air}}) \end{cases} \quad (A5)$$

C_d represents the aerodynamic drag coefficient, ρ represents atmospheric density, and S_1, S_2, S_3 represent the aerodynamic drag characteristic areas of the UAH1, UAH2 and suspended load, respectively.

References

1. Fang, Y. Development prospect of unmanned helicopter system. *Aeronaut. Sci. Technol.* **2021**, *32*, 35–40. [CrossRef]
2. Zhao, W.; Wang, Z.; Zhang, X.; Xiang, Q.; He, Y. A Review on Key Technologies of UAV for Epidemic Prevention and Control. *Unmanned Syst. Technol.* **2020**, *3*, 8–18. [CrossRef]
3. Thanapalan, K. Nonlinear controller design for a helicopter with an external slung load system. *Syst. Sci. Control Eng.* **2017**, *5*, 97–107. [CrossRef]
4. Ren, Y.; Li, K.; Ye, H. Modeling and anti-swing control for a helicopter slung-load system. *Appl. Math. Comput.* **2020**, *372*, 124990. [CrossRef]
5. Li, H.; Han, Y. Robust anti-sway technology for helicopter suspension based on fluctuation control. *J. Beijing Univ. Aeronaut. Astronaut.* **2024**, *5*, 1629–1638. [CrossRef]
6. Lee, T. Geometric control of quadrotor UAVs transporting a cable-suspended rigid body. *IEEE Trans. Control Syst. Technol.* **2017**, *26*, 255–264. [CrossRef]
7. Su, Z.; Chen, J.; Xing, Z. Research on cooperative transportation control technology with multi-unmanned helicopters. *Unmanned Syst. Technol.* **2022**, *5*, 33–42. [CrossRef]
8. Yang, Y. Modeling and Simulation of Helicopter Slung Load System Based on Multi-Body System. Master's Thesis, Nanjing University of Aeronautics and Astronautics, Nanjing, China, 2020. [CrossRef]
9. Kuře, M.; Bušek, J.; Vyhlídal, T.; Niculescu, S.-I. Algorithms for cable-suspended payload sway damping by vertical motion of the pivot base. *Mech. Syst. Signal Process.* **2021**, *149*, 107131. [CrossRef]
10. Zeng, J.; Kotaru, P.; Mueller, M.W.; Sreenath, K. Differential flatness based path planning with direct collocation on hybrid modes for a quadrotor with a cable-suspended payload. *IEEE Robot. Autom. Lett.* **2020**, *5*, 3074–3081. [CrossRef]
11. Cicolani, L.S.; Kanning, G. *Equations of Motion of Slung Load Systems with Results for Dual Lift*; NASA: Washington, DC, USA, 1990.
12. Cicolani, L.S. *Equations of Motion of Slung-Load Systems, Including Multi-Lift Systems*; NASA: Washington, DC, USA, 1992; Volume 3280.
13. Gao, J.; Zhang, F.; Huang, P.; Liu, Y. Observer-based second order sliding mode control for tethered quadrotor transportation. In *Proceedings of the 2021 IEEE International Conference on Real-Time Computing and Robotics (RCAR)*; IEEE: New York, NY, USA, 2021; pp. 1335–1342. [CrossRef]
14. Pizetta, I.H.B.; Brandão, A.S.; Sarcinelli-Filho, M. Cooperative load transportation using three quadrotors. In *Proceedings of the 2019 International Conference on Unmanned Aircraft Systems (ICUAS)*; IEEE: New York, NY, USA, 2019; pp. 644–650. [CrossRef]

15. Song, Y.; Wang, H. Modeling and analysis of multi-helicopter coordinate system with slung load. *J. Beijing Univ. Aeronaut. Astronaut.* **2013**, *39*, 1279–1285. [CrossRef]
16. Huang, J.; Wang, Y.; Ni, L. Design of cooperative payload lifting and anti-swing control for dual UAVs. *Comput. Integr. Manuf. Syst.* **2024**, *31*, 4096–4104. [CrossRef]
17. Xian, B.; Wang, G.; Cai, J. Nonlinear robust control design for multi unmanned aerial vehicles suspended payload transportation system. *J. Jilin Univ. Eng. Technol. Ed.* **2024**, *54*, 1788–1795. [CrossRef]
18. Oh, H.-S.; Tahk, M.-J.; Yoo, D.-W.; Lee, B.-Y. Robust stabilization technique for the leader steering slung-load system/using sliding mode control. *Int. J. Aeronaut. Space Sci.* **2018**, *19*, 932–944. [CrossRef]
19. Liang, X.; Wang, Y.; He, W.; Sun, N.; Fang, Y. Cooperative control for underactuated aerial transportation systems via the energy-based analysis. *Control. Theory Appl.* **2020**, *37*, 2473–2481. [CrossRef]
20. Shirani, B.; Najafi, M.; Izadi, I. Cooperative load transportation using multiple UAVs. *Aerosp. Sci. Technol.* **2019**, *84*, 158–169. [CrossRef]
21. Li, X.; Zhang, J.; Han, J. Trajectory planning of load transportation with multi-quadrotors based on reinforcement learning algorithm. *Aerosp. Sci. Technol.* **2021**, *116*, 106887. [CrossRef]
22. Liu, Y.; Zhang, F.; Huang, P.; Zhang, X. Analysis, planning and control for cooperative transportation of tethered multi-rotor UAVs. *Aerosp. Sci. Technol.* **2021**, *113*, 106673. [CrossRef]
23. Hua, X.; Chen, M.; Yong, K.; Liu, K. Event-triggered formation optimization-based cooperative control for a multiple quadrotor suspension transport system. *Chin. J. Eng.* **2024**, *46*, 1535–1543. [CrossRef]
24. Wei, Y.; Yu, Z.; Chen, X. Barrier Lyapunov function-based nonlinear cooperative control approach for dual-quadrotor slung load system. *Asian J. Control* **2025**, *27*, 357–372. [CrossRef]
25. Fu, C.; Sun, H.; Dai, L.; Xia, Y. Robust MPC-based trajectory tracking control for quadrotor UAV-slung load system. In *Proceedings of the 2024 43rd Chinese Control Conference (CCC)*; IEEE: New York, NY, USA, 2024; pp. 2826–2833. [CrossRef]
26. Sun, S.; Wang, X.; Sanalitro, D.; Franchi, A.; Tognon, M.; Alonso-Mora, J. Agile and cooperative aerial manipulation of a cable-suspended load. *Sci. Robot.* **2025**, *10*, eadu8015. [CrossRef]
27. Li, W.; Todorov, E. Iterative linear quadratic regulator design for nonlinear biological movement systems. In *Proceedings of the First International Conference on Informatics in Control, Automation and Robotics*; SciTePress: Setúbal, Portugal, 2004; pp. 222–229. [CrossRef]
28. Zhang, H.-J.; Gong, J.-W.; Jiang, Y.; Xiong, G.-M.; Chen, H.-Y. An iterative linear quadratic regulator based trajectory tracking controller for wheeled mobile robot. *J. Zhejiang Univ. Sci. C* **2012**, *13*, 593–600. [CrossRef]
29. Han, Y.; Li, R.; Zhang, Y. An optimal control method for trajectory tracking and swing suppression in helicopter-slung load system. *Int. J. Aeronaut. Space Sci.* **2025**, 1–14. [CrossRef]
30. Jasim, W.; Gu, D. Iterative linear quadratic regulator control for quadrotors leader-follower formation flight. *Int. J. Model. Identif. Control.* **2019**, *31*, 152–160. [CrossRef]
31. Roulet, V.; Srinivasa, S.; Fazel, M.; Harchaoui, Z. On global and local convergence of iterative linear quadratic optimization algorithms for discrete time nonlinear control. *J. Mach. Learn. Res.* **2025**, *26*, 1–85.
32. Xia, J.; Zhou, Z. Model predictive control based on iLQR for tilt-propulsion UAV. *Aerospace* **2022**, *9*, 688. [CrossRef]
33. Kong, N.J.; Li, C.; Council, G.; Johnson, A.M. Hybrid iLQR model predictive control for contact implicit stabilization on legged robots. *IEEE Trans. Robot.* **2023**, *39*, 4712–4727. [CrossRef]

Disclaimer/Publisher's Note: The statements, opinions and data contained in all publications are solely those of the individual author(s) and contributor(s) and not of MDPI and/or the editor(s). MDPI and/or the editor(s) disclaim responsibility for any injury to people or property resulting from any ideas, methods, instructions or products referred to in the content.